Basaltic Pulses and Lithospheric Thinning – Plio-Pleistocene Magmatism and Rifting in the Turkana Depression (East African Rift System)

Sahira M. Cancel Vazquez[1], Tyrone O. Rooney[1*], Eric L. Brown[2], Andrew Bollinger[1], Ian D. Bastow[3], R. Alex Steiner[1], John Kappelman[4].

[1]*Department of Earth and Environmental Science, Michigan State University, East Lansing, MI 48824, USA.*
[2]*Department. of Geoscience, Aarhus University, Denmark*
[3]*Department of Earth Science and Engineering, Imperial College London, London, UK*
[4]*Departments of Anthropology and Geological Sciences, University of Texas at Austin, Austin, TX, USA*

*corresponding author

Abstract

The East African Rift System provides an opportunity to constrain the relationship between magmatism and plate thinning. During continental rifting, magmatism is often considered a derivative of strain accommodation – as the continental plate thins, decompression melting of the upper mantle occurs. The Turkana Depression preserves among the most extensive Cenozoic magmatic record in the rift. This magmatic record, which comprises distinct basaltic pulses followed by periods of relative magmatic quiescence, is perplexing given the lack of evidence for temporal heterogeneity in the thermo-chemical state of the upper mantle, the nonexistence of lithospheric delamination related fast-wave speed anomalies in the upper mantle, and the absence of evidence for sudden, accelerated divergence of Nubia and Somalia. We focus on the Pliocene Gombe Stratoid Series and show how lithospheric thinning may result in pulsed magma generation from a plume-influenced mantle. By solving the 1D advection-diffusion equation using rates of plate thinning broadly equivalent to those measured geodetically today we show that despite elevated mantle potential temperature, melt generation may not occur and thereby result in extended intervals of quiescence. By contrast, an increase in the rate of plate thinning can generate magma volumes that are on the order of that estimated for the parental magma of the Gombe Stratoid Series. The coincidence of large-volume stratiform basalt events within the East African Rift shortly before the development of

axial zones of tectonic-magmatic activity suggests that the plate thinning needed to form these stratiform basalts may herald the onset of the localization of strain.

Plain Language Summary

The magmatic record in the Turkana Depression - part of the East African rift system - is characterized by pulses of basaltic activity that are followed by long periods of relative magmatic quiescence. This is a puzzling observation assuming that these magmas are generated by decompression melting of the upper mantle; there is no obvious changes in the rate of plate motion between Nubia and Somalia. This study presents new geochemical data on the final pulse of basaltic volcanism (during the Pliocene) and interprets these data in the context of a mantle melting model. We find that pulses of basaltic volcanism and intervening periods of quiescence could be simulated using different rates of thinning of the plate. We examine the consequences of a period of enhanced plate thinning in context of melt generation both below and within the plate.

1. Introduction

In a volcanic continental rift, magmatism is often considered a derivative of strain accommodation (e.g., Corti et al., 2003). Increased strain may facilitate the enhanced coupling of the brittle and ductile portions of the continental crust, thereby facilitating the transit of magmas and causing episodes of basaltic volcanism (e.g., Lahitte et al., 2003; Mazzarini et al., 2004). While such models do not directly consider the magma generation mechanisms, existing models of rift evolution outline a process whereby crustal transformation initially occurs by mechanical extension (e.g., Hayward and Ebinger, 1996), with magmatism typically acknowledged as a result of decompression melting of the upper mantle following lithospheric thinning (e.g., McKenzie and Bickle, 1988). However, observations from volcanic continental rifts highlight the typically pulsed nature of magmatism – large volumes of basalts may erupt in a discrete time window, followed by periods of either magmatic quiescence or lower volume silicic activity (e.g., Wilson et al., 2004; Rooney, 2020a; Guan et al., 2021). While the arrival or pulsing of a mantle plume into the sub-rift mantle is often invoked as a mechanism to explain some of these basaltic events (e.g., Ernst and

Buchan, 2003; Kitagawa et al., 2008; Rooney, 2017), evidence for discrete changes in the thermo-chemical conditions of the upper mantle associated with all such basaltic pulses is lacking (Rooney et al., 2012c). Thus, the conceptual relationship between pulses of basaltic magmatism and episodes of lithospheric thinning during rifting remains ambiguous (e.g., Karson and Curtis, 1989; Ebinger, 2005; Keir et al., 2013; Rooney, 2020a).

The East African Rift System (EARS) is the archetypal example of a volcanically active continental rift (e.g., Mohr, 1983; Hayward and Ebinger, 1996; Ebinger, 2005; Corti, 2009). Following Eocene-Oligocene flood basalt activity that is broadly linked to a mantle plume (e.g., George et al., 1998; Pik et al., 1999; George and Rogers, 2002; Krans et al., 2018; Steiner et al., 2021), distinct pulses of widely distributed basaltic magmatism in the EAR during the Early Miocene, Mid Miocene, and Pliocene have alternately been linked with episodes of lithospheric extension (Rooney, 2020a). The Turkana Depression has been recognized as an important locus of strain throughout the development of the EARS (Bonini et al., 2005; Morley, 2010; Macgregor, 2015; Purcell, 2018; Boone et al., 2019; Knappe et al., 2020; Morley, 2020; Rooney, 2020a). This region, which has been previously impacted by a failed episode of Mesozoic rifting (e.g., Bosworth and Morley, 1994; Vetel and Le Gall, 2006; Macgregor, 2015), forms a broad low-lying region located between the uplifted plateaus of Kenya and Ethiopia (Figure 1). Throughout the Cenozoic, episodes of magmatism and basin formation occurred within the Turkana Depression (Morley et al., 1999c; Wescott et al., 1999; Vetel and Le Gall, 2006; Furman et al., 2006; Boone et al., 2019; Cai et al., 2023), providing a window into the link between pulses of basaltic magmatism and episodes of lithospheric thinning during rifting.

This study focuses on a basaltic pulse that occurred in the Turkana Depression during the Pliocene. This magmatic event, which followed a ca. 5 Ma magmatic hiatus, is characterized by initial widespread fissural basalts (the Gombe Stratoid Series) and is followed by shield volcanism (Figure 1). Using major and trace element geochemistry and petrographic constraints, we investigate the petrogenesis of the Gombe Stratoid Series and Pliocene shield volcanism. We find that the Gombe Stratoid Series parental melts were generated by decompression melting of a plume-influenced upper mantle during a pulse of lithospheric thinning. During the shield volcanism phase, we find that magmatism becomes contaminated with enriched metasomatic components derived from the lithospheric mantle. We present a geodynamically-constrained 1D advection diffusion mantle melting model demonstrating that slow extension rates in the Turkana Depression following the Mid Miocene Resurgence would result in the conductive cooling of the upwelling mantle, preventing significant melt generation, and resulting in the observed magmatic hiatus in the Turkana Depression during this interval. We suggest that the termination of the magmatic hiatus by the eruption of the Gombe Stratoid Series results from a pulse of increased lithospheric thinning that permitted the underlying mantle to cross the critical melt generation threshold. We discuss the consequence of a pulsed thinning of the continental lithosphere in the context of how a modified geotherm may impact the stability of enriched, easily-fusible domains in the lithospheric mantle, and as a possible pre-cursor event prior to the modern-day focusing of strain and volcanism to discrete axial belts within the rift (Casey et al., 2006; Ebinger et al., 2017).

2. Background

2.1. Geologic History of the Turkana Depression

The Turkana Depression is located in the northern portion of the eastern branch of the EARS (Figure 1), encompassing approximately 131,000 km^2 of northern Kenya and southern Ethiopia (Furman et al., 2006; Feibel, 2011). The basin has been an important locality for the investigation of fossil-bearing sedimentary strata, with stratigraphic and geochronological studies (e.g., Boschetto et al., 1992; McDougall and Feibel, 1999; Gathogo et al., 2008; McDougall and Brown, 2008, 2009; Brown and McDougall, 2011) providing a well-developed chronostratigraphic framework of the region.

The metamorphic basement of the Turkana Depression mainly comprises deformed schists and gneisses that formed during the Pan-African orogeny (Brown and McDougall, 2011). These rocks are the main sediment source of the clastic sequences that were deposited in Late Mesozoic and Cenozoic extensional basins (Brown and McDougall, 2011; Feibel, 2011). Turkana has an extensive history of basin and rift development, creating its highly faulted morphology and thin continental crust (e.g., Hendrie et al., 1994; Ebinger and Ibrahim, 1994; Ebinger et al., 2000). The earliest evidence of rifting in the Turkana Depression is associated with the northwest-southeast trending Mesozoic Central African Rift System (CARS) (e.g., Bosworth, 1992; Feibel, 2011). During this period, the ~500 km long Anza Graben developed East of present-day Lake Turkana, with the oldest section of this rift being identified within the Chalbi Desert (Morley et al., 1999a). Gravity and seismic data have been used to study this rift system, as none of its structure is found at the surface due to coverage of Cretaceous-Paleogene sediments and Pliocene-Quaternary volcanics (Reeves et al., 1987; Simiyu and Keller, 1997; Morley et al., 1999a). Subsequent Cenozoic rifting (i.e., EARS) has resulted in the thinned crust that currently characterizes some parts of Turkana (e.g., 20 km in the Lake Turkana Basin; Mechie et al., 1997; Prodehl et al., 1997).

Cenozoic rifting in the Turkana Depression is characterized by an overall eastward migration of strain and magmatism (e.g., Morley et al., 1992; Ebinger et al., 2000; Vetel and Le Gall, 2006; Macgregor, 2015; Schofield et al., 2021), commencing west of Lake Turkana with the development of north-south trending Paleogene rift structures (Macgregor, 2015; Purcell, 2018). To the northwest of Lake Turkana, Oligocene volcanism marked the beginning of this new rift phase in the Turkana Depression (Morley et al., 1992). The oldest EAR rift basin in Turkana is the Paleogene-Miocene South Lokichar basin (also referred to as Lokichar basin in literature: Morley et al., 1999b). From this basin, rifting migrated eastwards to the North Lokichar, Kerio, and Lake Turkana basins (Morley et al., 1992, 1999b; Hendrie et al., 1994; Macgregor, 2015; Purcell, 2018). The modern locus of strain in the Turkana Depression is considered to be within and to the west of the Lake Turkana basin (Muirhead et al., 2022; Rooney et al., 2022; Musila et al., 2023).

Volcanism in the Turkana Depression initiated during the Eocene and has extended to Recent times (e.g., Ebinger et al., 1993, 2000; George et al., 1998; Furman et al., 2006; Brown and McDougall, 2011). Eocene to Oligocene volcanism was dominantly basaltic, though other volcanic products such as rhyolites and ignimbrites are also present (Furman et al., 2006; Brown and McDougall, 2011; Rooney, 2017). The best-characterized section of this period is located within the Lokitaung Gorge near to Lake Turkana (Steiner et al., 2021, 2024), but other sections are recorded from contemporary events in southern Ethiopia

(Davidson and Rex, 1980; Davidson, 1983; George et al., 1998; George and Rogers, 2002; Steiner et al., 2021). Subsequent magmatic activity in the Turkana Depression manifested as a series of basaltic pulses that are followed by relative magmatic quiescence or isolated silicic volcanism (Rooney, 2020a). The first basaltic pulse – the Early Miocene Resurgence Phase (ca. 24 - 17 Ma: Boschetto et al., 1992; Morley et al., 1992; McDougall and Watkins, 2006; Rooney, 2017, 2020a) – is considered the first instance of magmatism that extended into the growing Kenya Rift (Samburu Basalts), suggesting southwards migration of magmatism from Turkana towards this region (Rooney, 2020a). The second pulse of basaltic magmatism – the Mid Miocene Resurgence Phase (ca. 12 Ma - 9 Ma) – is characterized by widespread stratiform basalts (e.g., Lothidok, Nabwal Arangan Beds at Lothagam Hill, and south of Marsabit shield volcano: Brotzu et al., 1984; Bellieni et al., 1986; Key and Watkins, 1988; McDougall and Watkins, 1988; McDougall and Feibel, 1999; Rooney, 2020a). The final basaltic pulse, which is the focus on this study, commenced during the Pliocene at ca. 4 Ma.

2.2. Stratoid Phase – Gombe Group and Pliocene shield volcanism

After a ca. 5 Myr hiatus, a new pulse of magmatic activity began in the Turkana Depression, Southern Ethiopia, and in the Kenya Rift (Rooney, 2020a). This period also marks the recommencement of tectonic activity in the Turkana Depression, with studies (e.g., Macgregor, 2015; Purcell, 2018) suggesting the reactivation is linked with deepening of the rift. The Stratoid Phase (ca. 4 Ma – 0.5 Ma) initiated with the Gombe Stratoid Series – an aerially extensive basaltic event that is dated between 4.22 Ma – 3.97 Ma (Gathogo et al., 2008). These lavas flooded out into the basins, flowing unconformably over tilted and eroded Miocene volcanic and sedimentary units (e.g., Davidson, 1983). These evolved and compositionally homogenous lavas are dominantly aphyric and are remarkably flat-lying, being comprised of thick, continuous flows (~10 m) that are separated by thin sedimentary horizons (e.g., Watkins, 1986; Key and Watkins, 1988). These lavas are mainly exposed on the Suregei and Gombe Plateaus in the Turkana Depression (Figure 1) as well as in the Omo Valley (Mursi basalts) and small plateaus (Harr) in Ethiopia (Haileab et al., 2004). Other exposures east of Lake Turkana include those found in the Kokoi Highland where basaltic dikes intruded the Lonyumun Member of the Koobi Fora Formation (Haileab et al., 2004), and in the Ririba rift region (Franceschini et al., 2020). To the west of Lake Turkana, basalts such as those at Lothagam Hill have also been included as part of the Gombe Group by Haileab et al. (2004).

The areally extensive Gombe Series in the Turkana Depression was followed by spatially-limited basaltic activity in the form of shield volcanoes emplaced on top of the Gombe lava flows, with the main volcanic edifices located on the eastern shore of Lake Turkana: Longipi (3.5 - 1.5 Ma) (Furman et al., 2006), Kulal (3.01 - 1.71 Ma) (Ochieng et al., 1988; Gathogo et al., 2008), Asie (2.7 - 2.07 Ma) (Key et al., 1987), Marsabit shield (1.70 - 0.76Ma) (Key et al., 1987), and the Pliocene-Quaternary Huri Hills (Class et al., 1994). The volcanic edifices that followed the Gombe Group (Longipi, Kulal, Asie) located along the eastern side of Lake Turkana follow an en echelon arrangement (Figure 1). Younger monogenetic cones, maars and flows are located on top of the shields, whereas monogenetic fields of similar age occur between them (Key and Watkins, 1988; Class et al., 1994). These younger features extend to Ethiopia (Rooney, 2020a; Franceschini et al., 2020). Compositionally, the shields are made up of olivine-plagioclase phyric or clinopyroxene-olivine phyric basaltic flows. The Namarunu shield volcano in the Kenya Rift is associated with the Lorikipi Basalts (4.0 Ma – 2.33 Ma); these basalts are also considered linked to this shield building phase (Dunkley et al., 1993; Rooney, 2020a). In the Loiyangalani region, three basaltic units exist within the Koobi Fora Formation: the ca. 3.3 Ma – 3.2 Ma Kankam basalt, the Lenderit basalt (2.18 Ma – 2.02 Ma), and the 1.79 Ma Balo basalt (Gathogo et al., 2008). As presented by the authors, these basalts are correlated with the Pliocene shield-building phase.

3. Methods

3.1. Samples and sample preparation

This project was conducted using two sample suites that include rocks from the Gombe Stratoid Series lavas and the Pliocene shield volcanoes (Supplementary Information 1). The suite collected by Frank Brown consists of 25 samples from the Gombe Group lavas and 21 from the Pliocene Shields. The second sample suite used in this project was collected by Neil Opdyke (Opdyke et al., 2010). This suite contains 20 core samples from the Loiyangalani region that correspond to the Pliocene Shield-building phase. Geochemical data were collected for 15 of these samples, but all 20 samples were used to describe the petrography of the group they correspond to. High resolution thin section scans of samples from both suites were produced using PiAutoStage (Steiner and Rooney, 2021) to facilitate the petrographic analysis portion of this study.

To obtain major and trace element data, samples from the Brown suite were originally cut into billets and polished to remove saw marks. To eliminate any possible contamination, the samples were then cleaned in an ultrasonic bath using de-ionized water. These samples were powdered using a BICO flat plate pulverizer with ceramic plates. In contrast, core samples from the Opdyke suite were initially polished to remove contaminants in the surface of the cores. The samples were then crushed using the Sepor Model 150 Mini Jaw Crusher, and the sample chips were hand powdered using an agate mortar and pestle. For each sample, a homogeneous glass disc was fused using rock powder and lithium tetraborate flux, following the procedure of Rooney et al. (2012b).

3.2. Analytical Work

Geochemical analyses were conducted at Michigan State University using X-ray fluorescence (XRF) and laser ablation inductively coupled plasma mass spectrometry (LA-ICP-MS) for major and trace elements, respectively. The fused discs were analyzed for major elements using a Bruker S4 Pioneer XRF. The instrument was calibrated using rock standards that have also been fused into glass discs using the methods of Rooney et al. (2012b). The same sample discs were analyzed for trace elements using a Photon Machines Analyte G2 Excimer and Thermo iCAPQ Quadrupole ICP-MS and following the methodology of Rooney et al. (2014). These data were collected over a total of five sessions in which the standards were run multiple times as unknowns. Samples were ablated by a 193 nm laser (spot size: 110 microns) for a total of 120 seconds. Each sample was run three times and the individual runs were averaged to obtain trace element concentrations. In addition, each session included a sample replicate as part of the analysis, with a total of 5 replicates of different samples. Full analytical results and geologic standard information are available in the supplementary material.

4. Results

Our sample suite has been subdivided based on stratigraphy, petrology and geochemistry. The most prominent division is between the Gombe Stratoid Series and the subsequent Shield Volcanism. Given the somewhat limited geochemical variability of the Gombe Stratoid Series, an analysis of a wide range of samples from the group that is collected in the same analytical lab provides an opportunity to examine magmatic heterogeneity that may not otherwise be evident. Within the Gombe Stratoid Series we have created three subdivisons: (i) **Hoi Basalts** (Hoi) – first recognized by Bruhn et al. (2011), these basalts were a locally widespread event (60 x 120 km centered at 3°N, 37°E) that is older than the Gombe Basalts. While no radiogenic dates have been reported from this unit, we interpret it within the context of the broader Gombe Stratoid Series, which incorporates all magmatic units after the magmatic hiatus that followed the Mid Miocene Resurgence (Rooney, 2020a). (ii) **Gombe Basalts A** (Gombe A) – Lavas from this group typically have MgO > 4 wt % MgO. (iii) **Gombe Basalts B -** Lavas from this group typically have MgO ≤ 4 wt % MgO. Within the Shield Volcanism group, we discuss geochemical and petrographic variability based on individual volcanoes (Figure 1): Longipi, Kulal, Kankam, Lenderit, Balo, Asie, and Huri Hills. Three samples had a total sum of major elements that were below 95 % and exhibited signs of alteration (TOR0001DH; 1DF; 1DE) – these samples have been excluded from the plots and discussion.

4.1. Petrography

Lavas from the Gombe Stratoid Series (Hoi, Gombe A, Gombe B) are plagioclase and clinopyroxene-phyric, with oxides also present. Olivine was only identified in the Hoi basalt, where it is a minor phase. Despite these groups having the same mineralogical composition, two main textures have been identified: cotectic crystallization and glomerophyric texture (see Supplementary Material). Cotectic crystallization occurs as "bow-tie" plagioclase intergrowth with clinopyroxene (e.g., Bryan, 1979; Thy, 1983). This texture has been identified in the Hoi basalt, and it is also the main texture of Gombe A. The glomerophyric texture is found in Gombe B, where glomerocrysts are made up of clinopyroxene and plagioclase, but oxides are also common. Monomineralic (i.e., clinopyroxene or plagioclase) glomerocrysts are also seen in this group, but these are less abundant than the former. Some samples of the Gombe A group (6 out of 14; see

Supplementary Material) are also glomerophyric; these are made up of plagioclase and clinopyroxene, and unlike Gombe B, oxides are rare.

Lavas from the shield volcanism phase, in contrast to the preceding Gombe Stratoid series, are olivine-phyric, with plagioclase and/or clinopyroxene also being major phases in some groups (see Supplementary Material). Several textures have been identified among the shield volcanoes: microcrystalline (Longipi, Kulal, Kankam, Lenderit, Balo), porphyritic-coarse grained (Longipi), intergranular (all except Balo), ophitic (Kankam), and vesicular (Lenderit, Longipi, Balo, Asie, Kulal (1 sample)). Additionally, olivine occurs as glomerocrysts in samples from the Kankam basalt, Asie, and Huri Hills. Despite olivine being a major phase in the shield volcanoes, the Lenderit basalts are the only group from the shield volcanism phase in which plagioclase is the main phase and olivine and clinopyroxene are minor phases.

4.2. Geochemistry

All geochemical data and standard information have been uploaded to Earthchem (Cancel-Vazquez et al., 2024).

4.2.1. Gombe Stratoid Series

Major and trace element data of the Gombe A and B groups exhibit moderately evolved compositions, with 3.5-5.0 wt.% MgO. These lavas are also characterized by high TiO_2 (~3.2-3.8 wt. %), which is uncommon for other lavas in the region (see Rooney 2020a; Figure 2) and is noted as a diagnostic characteristic of these lavas (Halieab et al., 2004). An interesting feature of lavas from this region is the lack of a distinct break towards lower V concentrations at ~5-5.5 wt. % MgO (Figure 3) – a common feature further north in the Main Ethiopian Rift that is interpreted to be caused by crystallization of Fe-Ti oxides. Despite their overall "clustering", these two groups can be distinguished on the basis of their MgO content, as described below. Basalts from the Hoi group, in contrast, have slightly more primitive compositions than Gombe A and B (see below).

Hoi: Major and trace element data from the Hoi basalts show that they are slightly more primitive than Gombe A and B lavas, with 5.7-5.9 wt. % MgO (Figure 2). Hoi is also relatively high in TiO_2 (~3.0-3.5 wt.

%) in comparison to other regional basalts, however, they are lower in TiO_2 than the exceptionally high concentrations observed in Gombe A and B. When compared to Gombe A and B, the Hoi lavas plot along the same linear trend in incompatible trace element enrichment (Figure. 4).

Gombe A vs Gombe B: Lavas from Gombe A all have MgO > 4 wt. %, whereas Gombe B lavas have MgO ≤4 wt. %. Given the extremely limited range in MgO, other major elements are characterized by small variability and tight clustering. Gombe A lavas extend to slightly lower concentrations of Al_2O_3 and P_2O_5 and higher concentrations of Fe_2O_3 in comparison to Gombe B lavas. Compatible elements (Figure 3) show no distinct variations between the units. Incompatible trace elements show an increase in REE and other incompatible trace element concentrations – except Sr – with decreasing MgO (wt. %) (Figure 4), resulting in a slightly higher concentration of these elements in Gombe B.

Primitive mantle normalized diagrams (Figure 5) show peaks in Ba, Nb-Ta and negative anomalies in Th-U, K, Sr for Gombe A, B and Hoi basalts. Gombe A and B have similar levels of incompatible trace element enrichment, while the less differentiated Hoi basalts plot at lower values. The pattern for the Gombe A, Gombe B, and the Hoi basalts broadly represents a magma Type III pattern in the 6-fold division proposed by Rooney (2020b), and which is characterized by its peaks in Ba and Nb-Ta, and a trough in Th-U. As the lavas evolve (i.e., from Hoi to Gombe A to Gombe B), the trough in Th-U and peak in Nb-Ta flatten out to a straight line (Figure 5).

4.2.1.1. Characterization of textures in the Gombe Groups and their effect on geochemistry

As noted above, Gombe A dominantly exhibits cotectic texture while Gombe B is dominated by a glomerophyric texture (6 out of 7 samples). Despite this, glomerocrysts are still present in some samples that are part of the Gombe A group (6 out of 14 samples). To determine the abundance of glomerocrysts in Gombe A and Gombe B, a similar approach to that described by Humphreys et al. (2013) was used. Glomerocrysts were identified using ImageJ software (Schneider et al., 2012), where each glomerocryst was outlined by drawing a polygon around it to obtain its area. The area of each glomerocryst was given in pixels and was then converted to m^2 based on the amount of pixels per meter of the high resolution thin section scans (507,000 pixels/meter). In addition to quantifying the amount of glomerocrysts per thin section, this method allowed us to calculate the total area occupied by glomerocrysts per thin section (see Supplementary Information 2 for details). To do this, the individual areas of each glomerocrysts per sample were summed to obtain the total area of glomerocrysts in a given thin section. This value was then divided by the area of the thin section scan (0.0015 m^2) to obtain the area (%) occupied by the glomerocrysts in the thin section (see Supplementary Information 2).

A total of 137 glomerocrysts were identified in Gombe A group, whereas a total of 212 glomerocrysts were identified in the Gombe B group. Based on the area calculations, the total percentage of glomerocrysts in the Gombe A group is about 0.18%. In contrast, the total percentage of glomerocrysts in the Gombe B group is about 0.64% (Supplementary Information 2). These calculations show that despite glomerocrysts being present in both groups, they are significantly more abundant in Gombe B. It is important to note, however, that these values are minimum estimates rather than a full representation of each group, given that the thin sections available for this study are representative of a small portion of the sample/lava flow.

The differences in abundance of glomerocrysts between the two groups ultimately influence the whole rock geochemistry of these lavas. Accumulation of plagioclase and pyroxene will have an effect on the concentrations of Al and Ca, as these are major constituents of their chemical compositions. The higher abundance of phenocrysts made up of plagioclase and clinopyroxene, as well as monomineralic glomerocrysts of the same minerals, has resulted in an overprinting of the CaO and Al_2O_3 concentrations in Gombe B, making this group more enriched in these elements than Gombe A. Other minerals that may have an effect in the whole rock geochemistry are oxides. Transition metals, such as V, are favored in these minerals. When comparing the glomerocryst composition of both groups, we found oxides to be a common phase in glomerocrysts from Gombe B group, but rarely seen in glomerocrysts from Gombe A. The accumulation of oxides in Gombe B could thus explain the behavior of V (ppm), where there is a drop in the concentration of this trace element, but then begins to gradually increase as more evolved compositions are reached (Figure 3).

4.2.2. Shield volcanoes

<u>*Longipi shield*</u>*:* The Longipi shield exhibits primitive compositions with ~10 wt. % MgO for all samples

except for one (~6 wt. % MgO; Figure 2). Apart from the lower MgO (wt. %) sample, which plots along samples from the Kankam basalts (see below), Longipi samples appear to cluster in their major and trace element concentrations, except for CaO (wt. %) and Sr (ppm), where concentrations are more scattered (Figures 2, 4). Longipi shield basalts also have relatively unusual compatible element concentrations compared with other many other lavas from the region – notable high Cr, low Sc and V (Fig. 3). Primitive mantle normalized plots (Figure 5) show Ba and Nb-Ta peaks, as well as negative peak in U, K and Ti. However, there are certain samples that exhibit some deviations from the overall signatures previously described: two samples lack the Ba and negative U peaks, three show a peak in Sr, and one sample displays a peak in Nd. Despite these deviations, most samples from Longipi broadly follow a Type III magma pattern, but the lack of a Ba peak and negative U peak is more representative of a magma Type IV pattern (see: Rooney, 2020b).

<u>Kulal Shield</u>: Kulal shield shows more compositional variability than Longipi. These samples range between ~5-12 MgO (wt. %) (Figure 2) and show an overall decrease in compatible trace elements and an increase in most incompatible trace elements with decreasing MgO (wt. %) except Sr (ppm) (Figure 4). Compatible elements are characterized by low Sc and V (Fig. 3). Trace element patterns in primitive mantle normalized plots (Figure 5) for Kulal are characterized by Ba and Nb-Ta peaks, Th-U trough, as well as a negative K peak. The overall signatures exhibited by Kulal lavas are similar to a Type III pattern (Rooney, 2020b).

<u>Asie Shield</u>: The single sample from Asie has a primitive composition, with about 12 wt. % MgO (Figure 2). The primitive mantle normalized diagram for Asie is characterized by a Th-U trough and Nb-Ta peak (Figure 5). There is also a small peak in Ba, a slope break between K-La, peaks in Sr and Nd, and a negative anomaly in P. Although the Th-U trough and Nb-Ta peak are present, the lack of a distinct Ba peak suggests that Asie deviates from the Type III magma pattern, resembling more of a Type IV pattern (Rooney, 2020b).

<u>Huri Hills</u>: This sample exhibits a primitive composition (about ~10 wt. % MgO; Figure 2). The primitive mantle normalized pattern for Huri Hills is characterized by large peaks in Ba and Sr, as well as a Nb-Ta peak and Th-U trough (Figure 5). Other characteristics of this pattern include small peaks in La and Nd,

and negative anomalies in K, P and Ti. Except for the distinct Sr peak, Huri Hills exhibits a pattern that broadly represents Type III magmas.

Kankam Basalt: The Kankam basalts (located to the east and north of Loiyangalani in Figure 1) show the most compositional variability of any unit in this study (Figure 2). Notably, the Kankam samples with high (>8 wt. %) MgO are those that contain olivine cumulates, thus, the accumulation of this phase has likely resulted in such high MgO concentrations. Kankam basalts show an increase in major elements with decreasing MgO, except for CaO (wt. %) and Al_2O_3 (wt. %), where concentrations of the latter begin to decrease at ~6 wt. % MgO. Overall, Kankam shows an increase in incompatible elements and a decrease in compatible elements with decreasing MgO (wt. %) (Figures 3 and 4).

A distinct clustering of samples at ~6 wt. % MgO in major and trace element concentrations has been identified in the Kankam basalts (Figure 2). The Longipi shield sample with low MgO (wt. %) also plots within this Kankam cluster. The lack of clustering behavior in Kankam samples with higher MgO (>8 wt. %) could be attributed to olivine accumulation, but because of the overall compositional variability within Kankam, it is also possible that the clustered samples are representative of the same lava flow.

Kankam exhibits Ba and Nb-Ta peaks as well as the U-Th trough in primitive mantle normalized diagrams (Figure 5), the latter being steeper in magmas with >8 wt. % MgO. These lavas also exhibit a K negative anomaly and a pronounced peak in Nd. Samples with ~6 wt. % MgO exhibit a negative anomaly in Ti, which is not identified in the more primitive samples of this group. In contrast, samples with >8 wt. % MgO have a pronounced Sr peak that is not found in lavas with ~6 wt. % MgO. Some samples also exhibit a slight Zr-Hf anomaly, which deviates from the magma Type III pattern. Despite these minor deviations, which could indicate contributions from other sources, this group broadly follows a magma Type III pattern (Rooney, 2020b).

Lenderit Basalts: Lenderit lavas (located to the north of Loiyangalani in Figure 1 – See Gathogo et al., 2008 for finer scale location information) exhibit the most evolved compositions of the shield building phase (Figure 2). These flows range between ~2-7.6 wt. % MgO and have the highest TiO_2 (3-3.5 wt. %) content out of all the groups of the shield volcanism phase. The data for Lenderit are scattered, making it difficult to establish trends in major and trace elements. However, they exhibit a decrease in Al_2O_3 (wt. %) and CaO (wt. %), Sr (ppm) and compatible trace elements as samples become more evolved, but an increase in REE and other incompatible trace element concentrations (Figure 4). Trace element patterns in primitive mantle normalized plots (Figure 5) show Ba and Nb-Ta peaks, negative K and Ti anomalies and, with the exception of one sample where the pattern is flatter, a Th-U trough. There is also a Nd peak exhibited by all the samples, but there is variability in some of the signatures for Sr, P where some samples exhibit a negative anomaly and others do not. There are also some samples that exhibit an anomaly in Zr-Hf similar to Kankam. Despite these slight variations, Lenderit broadly follows a Type III magma pattern (Rooney, 2020b).

Balo Basalt: The Balo basalts are located northwest of Loiyangalani in Figure 1 – See Gathogo et al., 2008 for finer scale location information. Our single sample has a primitive composition (~7 wt. % MgO) and plots between the low (~6 wt. %) and high (> 8 wt. %) MgO samples of Kankam (Figures 3, 4, 5). The Balo basalt's primitive mantle normalized pattern (Figure 5) shows a peak in Ba and Nb-Ta, K negative peak, and a Th-U trough. This sample follows a Type III magma pattern (Rooney, 2020b), however, similar to Kankam and Lenderit, there is a distinct Zr-Hf trough that is not characteristic of Type III.

The observed Zr-Hf, P, and Ti negative anomalies in several Pliocene shields may indicate their source is influenced by melts of lithospheric mantle metasomes containing amphibole and accessory phases that retain these trace elements (i.e. zircon, apatite, and oxides respectively). Other Pliocene-Quaternary lavas from the Turkana Depression, although limited, exhibit these characteristic depletions, but their origin has not yet been fully explored (Furman et al., 2006; Cai et al., 2023). Most notably, the lavas that do exhibit these negative anomalies are also Type IV lavas, implying a linkage in their origin.

5. Discussion

5.1. Revised spatial distribution of the Gombe Stratoid Series

Pliocene stratiform basalts have long been recognized as widely distributed in the Turkana Depression and southern Ethiopia (e.g., Fitch and Miller, 1976). Early work noted the possible correlations between these Pliocene basalts (e.g., Davidson, 1983), however, it was Haileab et al. (2004) who first combined the various Pliocene volcanics (based on both age and chemical composition) to define the *Gombe Group basalts*. Rooney (2020a) further expanded the geographic range of the Gombe Group basalts, adding other Pliocene plateau basalts to the south and east of the Gombe Plateau into a new *Gombe Stratoid Series*. Here we expand upon the rationale for the creation of the Gombe Stratoid Series and adjust the extent and definition of the unit. Like the Gombe Group basalts of Haileab et al. (2004), the Gombe Stratoid Series comprises contemporaneous lavas in the Turkana Depression and southern Ethiopia that share a common geochemical signature (high TiO_2 and relatively low MgO). These criteria result in revised classification of samples assigned to the Gombe Stratoid Series (see Text S1 for detailed rationales and units).

5.1.1 Geochemical Variability of the Gombe Stratoid Series

For the groups where data are available, there is little variation in the composition of the lavas – lavas from the previously defined Gombe Group fully overlap lavas of Harr, Mursi, and Usno (Figure 6; Text S1). A notable difference is the Bulal basalts, which exhibit a greater compositional range than the Gombe Group, Harr, Mursi or Usno lavas, extending almost to the same MgO content as the Hoi Basalts (Figure 6). The Bulal basalts, however, fall along the same vectors as the Gombe Group, and overlap them; this suggests a continuity in magmatic processes. We thus amalgamate the Bulal basalts into the Gombe Stratoid Series despite the compositional heterogeneity noted above.

5.1.2 Volume of erupted lavas associated with the Gombe Stratoid Series

Previous studies have estimated a ~5000 km^3 volume for the Gombe Group Basalts (Haileab et al., 2004). However, new constraints on the thickness of the basalts in the Turkana Basin that are based on borehole data (Schofield et al., 2021), and our expanded definition of what now constitutes the Gombe Stratoid Series, requires a revision of this earlier estimate. The inferred geographic extent of the Gombe Stratoid Series is drawn based on: A) The outcrop, seismic and borehole evidence for the continuity of the Gombe

Stratoid Series from the South Turkana Basin and across Lake Turkana (Dunkelman et al., 1988; Morley et al., 1999b; Schofield et al., 2021); B) The references to the continuity of these units under fill within basins or plains (e.g., Davidson, 1983) or as erosional remnants of larger plateaus (Key et al., 1987). In these cases, we have extended the boundary of the Gombe Stratoid Series to the rift basin boundaries (Purcell, 2018) or the limits of the Quaternary fill on the existing geological maps. The southern boundary of the Gombe Stratoid Series is unclear given the ambiguity of the age of the undifferentiated Plateau basalts. We have therefore estimated the boundary as approximately half-way between the recognized Gombe Stratoid Series exposures and the next outcrop south of Marsabit, extending into Lake Turkana. Sub-polygons were created on the basis of mapped thickness information for the flows in each region and the boundaries are estimated (Supplemental Material). These data were used to generate estimates of the volume of the Gombe Stratoid Series within each polygon (Supplemental Material). Using these refined estimates, the total volume of lava erupted during magmatism of the Gombe Stratoid Series can be estimated to be ~5600 km^3.

Given the relatively evolved composition of the Gombe Stratoid Series lavas, a significant mass of material must have been removed and retained in the crust during differentiation. To assess the original magma volume and determine the approximate mass lost during crystallization of the Gombe Stratoid Series, we performed a generalized equilibrium crystallization model using sample TOR0001D8 as a starting point (Supplemental Information). Though this lava is from a shield volcano, it is among the most primitive liquid compositions reported in the region. We used Rhyolite MELTS (Gualda et al., 2012) at a constrained oxidation state of QFM and QFM +1 with an initial water content of 0.5 wt. % at different crustal pressures (0.2, 0.5, and 0.8 GPa). We report the proportion of solid and liquid in the system once the remaining liquid has reached an MgO content matching the Gombe Stratoid Series (~4 wt. %) (Supplemental Information). Given the range of possible conditions, the initial magma volume needed to produce the erupted lava volumes of the Gombe Stratoid Series of the order 15,500 – 18,500 km^3. The addition of ~170-200 m of mafic material (Table S3) to the crust would be expected to have negligible impact on bulk crustal V_P/V_S ratios, consistent with the ~ 1.74 average observed by the receiver function study of Ogden et al. (2023)

5.2. Mantle Source of the Gombe Stratoid Series

A critical aspect of melt production during the Gombe Stratoid Series is the thermo-chemical state of the mantle in this region. Incompatible trace element patterns of mafic lavas occurring throughout East Africa exhibit distinctive characteristics that help constrain the origin of the progenitor magmas (Rooney, 2020b). Six broad 'types' have been identified outlining a variety of lithospheric and sub-lithospheric reservoirs that contribute to magmatism in the EARS (Rooney, 2020b). Trace element patterns of the Gombe Stratoid Series are dominated by a Type III magma pattern; such magmas are derived from the asthenosphere and are considered to be a mixture between detached African lithosphere, plume material, and depleted mantle (Rooney et al., 2012a; Rooney, 2017, 2020b).

To determine the conditions of melt generation in the mantle (i.e. pressure, temperature, and composition), we used a trace element model (Kimura and Kawabata, 2014) that uses a Monte Carlo-based approach to forward modeling, where input parameters were changed within specified limits. Further constraints on magma generation and migration processes derive from major element models (Lee et al., 2009; Kimura and Kawabata, 2014), which constrain the P-T conditions where the melt was last in equilibration with the mantle. In continental rifts, these equilibration depths can be equivalent to the lithosphere-asthenosphere boundary (Chiasera et al., 2021). Due to the absence of primitive (>6 wt. % MgO) compositions in the Gombe Stratoid Series, we constrain these parameters using primitive compositions from the Pliocene shield volcanism that followed the Gombe Stratoid Series that also exhibit a Type III signature.

5.2.1. Conditions of Last Equilibration between Melt and Mantle

To determine the conditions at which the melt was equilibrated in the asthenosphere prior to extraction to conduits in the continental lithospheric mantle, we used the Si-Mg thermobarometer of Lee et al. (2009). This model uses the Si and Mg content of the magmas to estimate the pressure and temperature at which the magma was last in equilibrium with the mantle. Samples from the Pliocene shield volcanoes were chosen based on composition (e.g., MgO > 6 wt. %) and mineralogy; lavas that exhibited olivine accumulation or clinopyroxene and/or plagioclase fractionation were not modeled. Samples that only exhibited olivine fractionation were back corrected to primary compositions using the built-in olivine correction from Lee et al. (2009). Model constraints were chosen following the parameters detailed in Appendix B of Brown et al. (2022) and in Lee et al. (2009): Fo = 90, $K_D^{ol\text{-}liquid} = 0.3$ and variable values of Fe^{3+}/Fe_{total} of 0.05 and 0.15.

The resulting median melt equilibrium pressure condition from the Lee et al. (2009) thermobarometry model, given $Fe^{3+/}Fe_{total} = 0.05$, is 3.0 GPa, with a median temperature of 1503°C. Presuming an average lithosphere density (ρ) of 2900 kg/m^3 and acceleration due to gravity (g) of 9.81 m/s^2, we convert pressure (P) to depth (h) using the equation P = ρgh, resulting in a depth of melt equilibration of 105.5 km. Increasing Fe^{3+}/Fe_{total} to 0.15 yields lower median pressure and temperature estimates of melt equilibration of 2.5 GPa and 1453°C (see Table 1). This pressure corresponds to a depth of 87.9 km. Temperature results from Lee et al. (2009) were converted into mantle potential temperatures (T_P) using the equations of Putirka (2016) (Equations 12a-c and 14a-c). These equations provide three different alternatives for mantle potential temperature conversion, each using a different value for degree of melting (F). Therefore, the average T_P and F resulting from these equations were used. The resulting median mantle potential temperatures from the major element modeling are 1470 °C for $Fe^{3+}/Fe_{total} = 0.05$ and 1421 °C for $Fe^{3+}/Fe_{total} = 0.15$ (Table 1).

5.2.2. Conditions of Melt Generation

To determine the conditions at which the melt was generated in the mantle, the HAMMS trace element model (Kimura and Kawabata, 2014) was used. The sensitivity of incompatible trace elements to mantle melting aids in constraining the source composition and estimating the melting parameters (Kimura and Kawabata, 2014 and references therein). HAMMS is a forward model that can estimate the parameters involved in melt generation of a given primary magma composition: mantle potential temperature (T_P), water content, pressure (P), source depletion (CsDep), and source contamination (F_{cont}) (Kimura and Kawabata, 2014). CsDep represents the degree of mantle depletion given by the wt. % of basaltic melt extracted from the source, whereas F_{cont} represents the wt. % fraction of contamination present in the source. Given that we have identified Type III magmas in our samples, several lithologies (i.e., depleted mantle, African lithosphere, plume material: Rooney, 2020b) are involved in generating these magmas. For this reason, we have followed the procedure detailed in Chiasera et al. (2021) to establish the source melt and contaminant lithologies to use in HAMMS (see Supplementary Text S2).

The conditions of melt generation that produce primary magmas that best match our samples are the following: T_P = 1390-1450 °C, P = 2.9-3.5 GPa, CsDep = 0.1-0.8 and F_{cont} = 1.0-4.0. Using the pressure results, the depth at which these melts were generated range from about 102 – 123 km (Table 1). The results of trace element source models indicate that initial mantle melting occurred at a depth of ~102-123 km with T_P = 1390-1450 °C. These melts migrate to and equilibrate at shallower depths ranging from ~74-133 km (Table 1) at similarly elevated mantle potential temperatures. This depth is consistent with a thinned tectonic plate in the region (Kounoudis et al., 2021).

Our results that show elevated mantle potential temperatures are consistent with previous estimates of mantle potential temperature in the Turkana Depression (Rooney et al., 2012c). These elevated temperatures have been attributed to the widescale pollution of the East African upper mantle by material derived from the African Superplume (Rooney et al., 2012c; Rooney, 2020b). The influence of the African Superplume on the upper mantle is evident in the earliest lavas erupted in this region. These Eocene lavas display Type III trace element lava patterns, which are characteristic of melts of a plume-influenced asthenosphere source (Rooney, 2020b). The isotopic characteristics of these lavas resemble that of the plume with high ε_{Nd} (4-6) and moderate $^{206}Pb/^{204}Pb$ ratios (19-19.5) (Furman et al., 2006; Cai et al., 2023), further supporting the contribution of a mantle plume to early Turkana magmatism. Since the Eocene, Type III lavas in the Turkana Depression have continued to display isotopic signatures consistent with a plume-influenced upper mantle, indicating that a mantle plume has been a prevalent feature of the Turkana Depression upper mantle throughout the Cenozoic. When this consistently hot asthenosphere is considered within the context of the pulsed nature (and even quiescence) of magmatic activity in the Turkana Depression, it raises questions about the mechanisms of melt generation during these magmatic intervals.

5.3. The Relationship between Rifting and Magmatism in the Turkana Depression during Miocene to Pliocene times.

5.3.1 Rifting, basin development and magmatism

From the Mid Miocene Resurgence at ca. 10 Ma (Rooney, 2020a) until the eruption at ca. 4.2 Ma of the Gombe Stratoid Series, basaltic magmatism in the Turkana Depression is lacking (e.g., Brown and McDougall, 2011). This extended interval of magmatic quiescence is perplexing given that rifting continued during this period. Field constraints demonstrate that Miocene strata are tilted and eroded prior to the eruption of the Gombe Stratoid Series (Davidson, 1983). Significant Upper Miocene sediment accumulation is reported from seismic and borehole constraints in the North Lokichar Basin (>1 km), South Turkana Basin, and North Kerio Basin (~600m), with a pronounced thickening of 10 – 6 Ma sediments into the Lokichar Fault (Schofield et al., 2021). These data provide clear evidence that extension was underway in Turkana during the Mid-Late Miocene magmatic hiatus, centered east of Lake Turkana. Presuming such extension manifested as plate thinning during this interval, magma generation by upwelling and decompression melting might be expected given that: (1) the mantle beneath most of East Africa is influenced by the African Superplume (Rooney, 2020b; Boyce et al., 2023), resulting in persistently elevated mantle potential temperatures (Rooney et al., 2012c); and (2) the lithosphere of the Turkana

Depression was already thinner than most regions of the EARS due to a prior episode of Mesozoic rifting (Dunkelman et al., 1988; Kounoudis et al., 2021, 2023).

The sudden reemergence of basaltic volcanism during the Pliocene in the Depression has been previously suggested to have resulted from an increase in tectonic activity (Watkins, 1986; Haileab et al., 2004) that thinned the continental lithosphere (e.g., Morley et al., 1992; Hendrie et al., 1994). This hypothesis is supported by evidence of a notable increase in tectonic activity during the Pliocene in the Depression, which was likely caused by changes in lithospheric stress conditions (Purcell, 2018). During the Pliocene, the extension direction is thought to have rotated north-east from its former east-west configuration (Vetel and Le Gall, 2006). The change in lithospheric stress conditions during Pliocene also impacted the location of basin development in the Turkana Depression. While prior episodes of basin formation centered on the regions located to the west of Lake Turkana (e.g., Lokichar Basin: Morley et al., 1999b), the Pliocene brought a new phase of basin development associated with the northward migration of strain from the Kenya Rift; this manifested in the Turkana Depression as the Turkana Basin (Vetel and Le Gall, 2006; Muirhead et al., 2022) (Figure 1). Similarly, the eastward migration of strain from the Omo basin during the Pliocene manifested as the Segen basin and Ririba Rift (e.g., Ebinger et al., 2000; Corti et al., 2019). While the footprint of the Gombe Stratoid Series overlaps these newly active Pliocene basins (Figure 1), the eruption of the Gombe Stratoid Series clearly preceded basin development: Gombe Stratoid Series lavas erupted onto flat surfaces, are cut by rift bounding faults (Corti et al., 2019), and are not observed to thicken into the basin bounding faults (Schofield et al., 2021). These observations suggest broad lithospheric thinning during the Pliocene manifested as a widespread pulse of basaltic volcanism followed by basin development.

5.3.2 A thermo-mechanical model for magmatism in the Turkana Depression

Given the geophysical evidence that extension in the Turkana Depression (prior to the modern axial phase: e.g., Morley, 1994; Muirhead et al., 2022; Morley, 2020; Boone et al., 2019) is dominantly accommodated through mechanical processes and not magma intrusion, we assume a direct relationship between extension and plate thinning. The rate at which the plate thins may play an important role in magma generation. Specifically, we hypothesize that while extension and plate thinning was ongoing during the Mid to Late Miocene, the rate plate thinning was sufficiently slow so as to permit conductive cooling of the upwelling asthenosphere, thereby suppressing mantle melting. We further hypothesize that an increase in the rate of plate thinning during the Pliocene (e.g., Macgregor, 2015; Purcell, 2018) may produce a pulse of basaltic magmatism.

To explore and test these hypotheses, we have constructed a 1D thermo-mechanical model that simulates mantle melting caused by decompression of the asthenosphere (Supplemental Text S3). The mechanical aspects of the model depend on asthenospheric decompression, which results from changes in the position of the lithosphere-asthenosphere boundary in response to plate thinning. The thermal aspects of the model depend on asthenospheric temperature, and how this changes as a consequence of mantle upwelling, conductive cooling to the lithosphere, and melt generation. We solve the 1D advection-diffusion equation assuming constant horizontal velocity and accounting for the latent heat effects of melting (Pedersen and Ro, 1992; Pedersen and van der Beek, 1994).

We have explored a range of mantle potential temperatures (T_P) for the upper mantle beneath the Turkana Depression (1400-1450°C), consistent with our modeling results and independent studies (Rooney et al., 2012c), and plate thinning resulting from a background half extension rate of 2 mm yr^{-1}, broadly consistent with current geodetically constrained plate motion measurements (Knappe et al., 2020; Musila et al., 2023). We assume that the initial width of the extending region is 100 km – the approximate width of the N. Lokichar and Keiro basins where extension commenced during the Oligo-Miocene (Schofield et al., 2021). To ensure no melting occurred at the onset of the model, the initial lithosphere thickness was taken to be 1 km deeper than the intersection of the mantle adiabat (specified by a given mantle potential temperature) and the peridotite solidus (Katz et al., 2003). Using this constraint, the initial lithosphere-asthenosphere boundary in the model ranged from ~100 to 120 km. We commenced the simulation when the steady state conditions become perturbed – i.e., at the onset of Cenozoic rifting in the region ca. 30 Ma, and monitor the cumulative thickness of basaltic melt produced and lithospheric thickness as a function of time.

We first tested the null hypothesis whereby plate thinning was achieved in our model by imposing a constant rate of extension (2 mm y^{-1}). The outcome of these initial models was a paucity of melt generation, despite substantial lithospheric thinning (β ~ 1.6 – not dissimilar to the 1.51-1.79 range constrained by crustal receiver function analysis: Ogden et al., 2023) and elevated values of T_P. In these models, melt is only recorded at the hottest values of T_P, and only in small amounts (maximum cumulative melt thickness ~20 km) after ca. 10 Ma. These results are inconsistent with observations of substantial accumulations of basaltic melt in the Turkana Depression throughout the Cenozoic (Fig. 7 a-c).

We then implemented a pulsed plate thinning scenario by imposing a background extension rate (2 mm yr^{-1}) that was increased to a maximum value (6 mm yr^{-1}) and returned to the background rate using a gaussian function (Fig. 7d-f). In practice, this assumed extension rate exceeds expected long-term Nubia-Somalia separation rates. However, the accelerated thinning rates could be equivalently achieved by diachronous stretching of the lithosphere or a narrowing of the extending zone in our model, or both. We implemented three periods of pulsed plate thinning in order to generate the temporal extent of the recognized basaltic pulses in the region (Brotzu et al., 1984; Rooney, 2020a). The outcome of this approach is a modestly higher degree of lithospheric thinning (β ~ 1.9) when compared to the steady state approach, but a substantial increase in both the magnitude and temporal extent of magma generation (Fig. 7 d-f). Importantly, the model demonstrates that melt generation occurred during the three pulses of plate thinning but was insignificant during periods governed by the background plate thinning (Fig 7f). Cumulative basaltic melt thicknesses for the pulse associated with Gombe magmatism (4.3 to 3.8 Ma) vary from ~1.5 m (T_P = 1400 °C) to ~30 m (T_P = 1450 °C). These melt thicknesses are too low when compared to the inferred thicknesses based upon corrected stratigraphic observations (~170 m - Table

S3). Modification of T_P to values higher than 1450°C could produce additional melt thickness, but the model results are inconsistent with the observed hiatuses in basaltic volcanism; at higher T_P, melt production becomes continuous.

We explored model parameters to establish a solution that matches the estimated melt thicknesses (based on stratigraphic constraints: Table S3). Even when the rate of plate thinning accelerated to ~3.5 km/Myr, these models yielded melt thickness only 33% of the estimated values (Figure 8c). Retaining this higher rate of plate thinning for the Gombe event, we then varied the pulse duration, finding that we can match the inferred melt thicknesses if the Gombe event lasted from ~5.8-3.6 Ma (Figure 8d-f). A longer duration episode for the Gombe event is consistent with the expanded definition of the Gombe Stratoid Series we have presented. The inclusion of the Bulal and Plateau basalts in addition to the older (but as yet, undated) Hoi basalts points to a potentially more significant temporal extent of magmatism defining the Gombe event. Given the range of potential solutions possible in our model by simultaneously adjusting the duration and magnitude of the extension, additional geochronological constraints and estimates of magma crustal residence time will be necessary to fully constrain the Gombe event. Nevertheless, our modeling demonstrates clearly that it is possible to generate pulsed basaltic magmatism during the Mid to Late Miocene; plate thinning between magmatic pulses was sufficiently slow to suppress mantle melting. We further show that within the parameter space we have explored, pulsed magmatism requires intervals of increased rates of plate thinning.

5.4 Implications of a Pliocene pulse of lithospheric thinning

Our models demonstrate that the Miocene hiatus in magmatism in the Turkana Depression likely results from relatively low rates of plate thinning. Advective cooling of the upwelling mantle suppresses magma generation. The eruption of the Pliocene Gombe Stratoid Series requires an increase in the rate of plate thinning and associated magma generation over a broad zone. This thinning subsequently impacted the position of the geotherm within the continental lithospheric mantle, causing the thermo-baric destabilization of enriched domains within it. Corroborating this model prediction, the post-Gombe Stratoid Series shield shows clear evidence for metasome destabilization.

This sequence of a lithospheric thinning event yielding a pulse of basaltic volcanism and subsequent melts of the continental lithospheric mantle is repeated elsewhere in the EAR. An episode of plate thinning in Afar during the Late Miocene (Wolfenden et al., 2005; Stab et al., 2016) resulted in an episode of basaltic volcanism followed that was accompanied by the thermal re-equilibration of the lithospheric mantle. The shallowing of the geotherm following this thinning event resulted in the destabilization of enriched, easily fusible domains hosted within the continental lithospheric mantle, resulting in magmatism with the clear signature of melts derived from the continental lithospheric mantle (Rooney et al., 2023).

The commonality in magmatic processes in the Afar and Turkana Depressions extends beyond that of pulsed lithospheric thinning events. Within the eastern branch of the EAR, the period beginning in the Pliocene and lasting until modern times is characterized by a shift from more widely distributed magmatism towards zones of focused intrusion located on the floor of the rift. In parts of the rift, such as the MER and Afar, this shift is accompanied by a change in strain distribution such that zones of focused tectonic and magmatic activity are accommodating most of the extensional stresses that manifest in these regions (e.g., Hayward and Ebinger, 1996; Ebinger and Casey, 2001; Casey et al., 2006). In the Turkana Depression, this transition is also underway – the modern axis of extension is now located largely in the Lake Turkana Basin (Knappe et al., 2020; Muirhead et al., 2022; Rooney et al., 2022). Consistent with the requirement in our models for a reduction in the rate of plate thinning at the end of the Gombe Stratoid Series, axial extension commences along and to the west of the Lake Turkana Basin. Modern extension is therefore not being achieved by plate thinning but instead by magma-assisted rifting. Given the commonality in the both the mechanism and sequence of magmatism in Afar and Turkana, we suggest that the thinning of the plate necessary to generate these basaltic pulses may also represent a critical precursor event that signals the beginning of strain localization in axial regions on the rift floor.

6. Conclusions

Magmatism during the Miocene and Pliocene in the Turkana Depression is characterized by distinct basaltic pulses followed by periods of magmatic quiescence. The Gombe Stratoid Series, which form a laterally extensive group of lavas that are characterized by limited compositional heterogeneity, marked the recommencement of volcanic activity in the Turkana Depression after a long period of Miocene magmatic quiescence. The existence of these basaltic flows is perplexing given: (1) The lack of evidence for significant temporal heterogeneity in mantle thermo-chemical conditions; (2) The absence of fast wave-speed upper mantle anomalies that could be attributed to recent lithospheric dripping/delamination (Kounoudis et al., 2021); (3) a lack of evidence for abrupt accelerated Nubia-Somalia divergence. The Gombe Stratoid Series lavas provide a window as to how lithospheric thinning may result in pulsed magma generation processes in the Depression during this period. By solving the 1D advection-diffusion equation using rates of plate thinning broadly equivalent to those measured geodetically today, we show that despite elevated mantle potential temperature melt generation may not occur, leading to extended intervals of magmatic quiescence.

We show that the Gombe Stratoid Series parental magmas were derived by decompression melting of the plume influenced upper mantle, subsequently undergoing magmatic differentiation within the overlying plate. By modifying the 1D advection-diffusion mantle melting model that we initially implemented to simulate the Miocene period of magmatic quiescence, we can simulate a pulse of magma generation. Within our modified model, an increase in the rate of plate thinning can generate magma volumes that are on the order of that estimated for the parental magma of the Gombe Stratoid Series. The thinning of the plate in the Turkana Depression during the Miocene is expected to have steepened the geotherm within the continental lithospheric mantle. Where this process has occurred elsewhere within the East African Rift System (e.g., Afar), melting of enriched domains of the lithospheric mantle has followed (Rooney et al., 2023). Our observation of a continental lithospheric mantle signature in magmatic activity subsequent to the Gombe Stratoid Series event (i.e., the shield volcanism overlying the Gombe Stratoid Series and modern axial activity in the Lake Turkana Basin) supports our model of lithospheric thinning associated with the generation of the Gombe Stratoid Series.

The eruption of the Gombe Stratoid Series and equivalent magmatism in Afar (Afar Stratoid Series) and the Main Ethiopian Rift (Bofa Stratoid Series) occurs shortly before the development of axial zones of tectonic-magmatic activity along the rift floor. This shift in the mechanism of strain accommodation is consistent with the termination of large-scale basaltic volcanism – the thinning of the plate necessary to achieve the volume melts has largely terminated and is replaced with magma-assisted rifting. We suggest that the thinning of the plate necessary to permit the eruption of these stratoid lavas may, in fact, therefore herald the onset of the localization of strain to narrow, axial zones of magma-dominated extension on the rift floor.

Acknowledgements

This project would not have been possible without access to the samples provided by very generous colleagues. We are deeply indebted to the kindness of the late Neil Opdyke and late Frank Brown who both provided samples to us. We thank David Foster and Dennis Kent for helping us with the transfer of these samples. This project was supported by an award from the United States National Science Foundation (1850606). We thank Francesco Mazzarini and an anonymous reviewer for formal peer review that helped improve the quality of this work. We thank Mark Dekkers for careful editorial handling.

Open Research

Geochemical data used in this paper can be found in the Earthchem repository (Cancel-Vazquez et al., 2024).

List of Figures

Figure 1

Stratoid and shield volcanism in the Turkana Depression, a low-lying zone between the Kenya Rift and Main Ethiopian Rifts. The behavior of magmatism in this time period is characterized by a dislocation between events, where modern axial activity is not co-located with the Pliocene Stratoid Phase. The Gombe Stratoid Series distribution is derived from: A) the Gombe Group basalt map of Haileab et al. (2004), B) The GIS shapefiles of Guth (2013), C) The sketch map of Corti et al. (2019), D) The Geological Map of the Konso – Yabello area (JICA, 2012). The shapefiles of Guth (2013) have been redesignated based on the Geological maps of the Turkana region and the rationales outlined within the main text for assignation of units to the Gombe Stratoid Series. For the Bulal Basalts, we have extended the extent of the unit northward into Southern Ethiopia based on the work of Corti et al. (2019) and using the map of Konso-Yabello. Where the boundary with another mapped unit is unclear (e.g., 4.5°N, 37.25°E), we have placed the boundary roughly equidistant. It is possible that the Bulal Basalts extend further north than shown here, however the existing mapping and geochemical data do not permit a confident assignment of other units. The inferred extent of the Gombe Stratoid Series is drawn based on: A) The outcrop, seismic and borehole evidence for the continuity of the Gombe Stratoid Series from the South Turkana Basin and across Lake Turkana (Dunkelman et al., 1989; Morley et al., 1999b; Schofield et al., 2021), B) The references to the continuity of these units under fill within basins or plains (Davidson, 1983) or as erosional remnants of larger plateaus (Key et al., 1987). In these cases, we have extended the boundary of the Gombe Stratoid series to the rift basin boundaries (Purcell, 2018) or the limits of the Quaternary fill on the map. The southern boundary is unclear given the ambiguity of the age of the Undifferentiated Plateau basalts. Note that the Undifferentiated Plateau basalts are basalts that may be assigned to either the Pliocene Stratoid Phase or the prior Mid Miocene Resurgence event. They are amalgamated into a single unit here as we have insufficient information on the age or composition of these basalts to subdivide them further. We have therefore estimated the boundary as about half way between the recognized Gombe Stratoid Series exposures and the next outcrop south of Marsabit, extending into Lake Turkana. Volcano locations based on the Smithsonian catalog. Faults are those presented by Macgreggor (2015). KSFB = Kino Sogo Fault Belt. Numbers refer to sample localities (see supplemental information).

Figure 2

Selected major element geochemistry for Gombe Stratoid Series and Shield Volcanism phase. Note the overall compositional homogeneity of the Gombe Stratoid Series and the variable compositions of the Pliocene shields. FeO is not total iron but is calculated based on an assumption that 15% of the total Fe is in the form of Fe^{3+} and 85% in Fe^{2+}. Data are derived from this publication.

Figure 3

Selected compatible trace element geochemistry for the Gombe Stratoid Series and Shield volcanism phase. Data are derived from this publication.

Figure 4

Selected incompatible trace element geochemistry for the Gombe Stratoid Series and Shield volcanism phase. Data are derived from this publication.

Figure 5

Primitive mantle normalized diagrams (Sun and McDonough, 1989) of the Gombe Stratoid Series groups and the Pliocene Shields.

Figure 6

Combined data for the Gombe Stratoid series. These data include rocks from this study in addition to published datasets (Asfaw et al., 1991; Stewart and Rogers, 1996; Haileab et al., 2004; Bruhn et al., 2011; Shinjo et al., 2011; Corti et al., 2019). Note that the lava names were assigned based on the location of eruption.

Figure 7

Results of our modelling of mantle melting due to thinning of the continental lithosphere. Full model parameters are presented in Text S3. A) Rate of plate thinning in a steady state model assuming a modern day geodetically observed extension rate (Knappe et al., 2020). B) Impact on lithospheric thickness through time given a rate of plate thinning governed by the modern rate of extension. Note that the hypothetical lithospheric thicknesses differ depending on mantle T_P as the initial lithosphere thickness ($z^0_{lithosphere}$) was taken to be 1 km deeper than the intersection of the mantle adiabat in order to prevent melt generation at the onset of the model. See text S3. C) Melt thickness produced over time depending on the mantle T_P. D) Our hypothesized pulsed lithospheric thinning model showing increases to the rate of plate thinning for intervals as shown. The plate thinning rate returns to the modern day background rate in between pulses. E) Impact of the variable lithospheric thinning rate rate on the change in lithospheric thickness through time. F) Melt thickness produced over time depending on the variable thinning of the lithosphere and mantle T_P.

Figure 8

Results of our modelling of mantle melting due to extension and thinning of the continental lithosphere. Full model parameters are presented in Text S3. A) This figure shows a pulsed lithospheric thinning model, however rate of lithospheric thinning during the Gombe event has been increased ~3.5 km/Myr. B) Impact of the variable lithospheric thinning rate on the change in lithospheric thickness through time. C) Melt thickness produced by variable lithospheric thinning rate over time for a mantle T_P of 1450°C. D) The interval of increased lithospheric thinning correlating to the Gombe event has been expanded to 5.8 Ma. The initiation of Gombe-related magmatism is not well constrained (see main text). E) Impact of the variable lithospheric thinning rate on the change in lithospheric thickness through time. F) Melt thickness produced by variable lithospheric thinning rate (and a longer Gombe event interval) over time for a mantle T_P of 1450°C.

Table 1

Thermobarometry results using the major element model of Lee et al. (2009) and Hydrous Adiabatic Mantle Melting Simulator (HAMMS) of Kimura & Kawabata (2014). See supplementary information for full modeling methods. Both pressure and temperature in this table has been calculated in three different ways – firstly using the major element model of Lee et al. (2009), then using the major element model of HAMMS and then the trace element model of HAMMS. Pressure is converted to depth with an approximation of 1 GPa = 30 km. T_P = Mantle potential temperature. For the HAMMS modelling the methods of Chiasera et al. (2021) were followed. Each of the six sample compositions (corrected to primary values – see supplementary information) were compared to synthetic model results derived from inputs reflecting varying mantle compositions using the pyroxenite AG7 as a contaminant (0-2% Fcont/%), variable pressures of final melting (2.5-3.5 GPa Pmt/GPa), varying mantle potential temperature of final melting (1400°C – 1450°C T_P/C), variable water content (0-1% H2O(i)/%) and variable source depletion (0-1%

CsDep/%ext). The initial conditions that most closely match the sample compositions are shown in the table.

REFERENCES

Asfaw, B., Beyene, Y., Semaw, S., Suwa, G., White, T., and WoldeGabriel, G., 1991, Fejej: a new paleoanthropological research area in Ethiopia: Journal of Human Evolution, v. 21, p. 137–143.

Bellieni, G., Brotzu, P., Morbidelli, L., Piccirillo, E.M., and Traversa, G., 1986, Petrology and Mineralogy of Miocene Fissural Volcanism of the East Kenya Plateau: Neues Jahrbuch Fur Mineralogie-Abhandlungen, v. 154, p. 153–178.

Bonini, M., Corti, G., Innocenti, F., Manetti, P., Mazzarini, F., Abebe, T., and Pecskay, Z., 2005, Evolution of the Main Ethiopian Rift in the frame of Afar and Kenya rifts propagation: Tectonics, v. 24, p. TC1007, doi: 10.1029/2004TC00168.

Boone, S.C., Kohn, B.P., Gleadow, A.J., Morley, C.K., Seiler, C., and Foster, D.A., 2019, Birth of the East African Rift System: Nucleation of magmatism and strain in the Turkana Depression: Geology, v. 47, p. 886–890.

Boschetto, H.B., Brown, F.H., and McDougall, I., 1992, Stratigraphy of the Lothidok Range, northern Kenya, and K/Ar ages of its Miocene primates: Journal of Human Evolution, v. 22, p. 47–71.

Bosworth, W., 1992, Mesozoic and Early Tertiary Rift Tectonics in East-Africa: Tectonophysics, v. 209, p. 115–137.

Bosworth, W., and Morley, C.K., 1994, Structural and stratigraphic evolution of the Anza rift, Kenya: Tectonophysics, v. 236, p. 93–115.

Boyce, A., Kounoudis, R., Bastow, I.D., Cottaar, S., Ebinger, C.J., and Ogden, C.S., 2023, Mantle wavespeed and discontinuity structure below East Africa: Implications for Cenozoic hotspot tectonism and the development of the Turkana Depression: Geochemistry, Geophysics, Geosystems, v. 24, p. e2022GC010775.

Brotzu, P., Morbidelli, L., Nicoletti, M., Piccirillo, E.M., and Traversa, G., 1984, Miocene to Quaternary volcanism in eastern Kenya: sequence and geochronology: Tectonophysics, v. 101, p. 75–86.

Brown, F.H., and McDougall, I., 2011, Geochronology of the Turkana depression of northern Kenya and southern Ethiopia: Evolutionary Anthropology: Issues, News, and Reviews, v. 20, p. 217–227.

Bruhn, R.L., Brown, F.H., Gathogo, P.N., and Haileab, B., 2011, Pliocene volcano-tectonics and paleogeography of the Turkana Basin, Kenya and Ethiopia: Journal of African Earth Sciences, v. 59, p. 295–312.

Bryan, W., 1979, Regional variation and petrogenesis of basalt glasses from the FAMOUS area, Mid-Atlantic Ridge: Journal of Petrology, v. 20, p. 293–325.

Cai, Y., Mana, S., Cox, S.E., Beck, C.C., Feibel, C., Hanley, J., Liu, T., Bolge, L., Hemming, S., and Goldstein, S.L., 2023, Geodynamic Evolution of the East African Superplume: Insights from volcanism in the western Turkana Basin (Merry): Journal of Geophysical Research: Solid Earth, p. e2023JB026755.

Cancel-Vazquez, S.M., Rooney, T.O., Bollinger, A.R., and Steiner, R.A., 2024, Gombe Series and Pliocene Shield Basalts from the Turkana Depression, Kenya, East African Rift [dataset]:, doi:10.26022/IEDA/113041.

Casey, M., Ebinger, C., Keir, D., Gloaguen, R., and Mohamed, F., 2006, Strain accomodation in transitional rifts: Extension by magma intrusion and faulting in Ethiopian rift magmatic segments, *in* Yirgu, G., Ebinger, C., and Maguire, P. eds., The Afar Volcanic Province within the East African Rift System, London, Geological Society, London, v. 259, p. 143–164.

Chiasera, B., Rooney, T.O., Bastow, I.D., Yirgu, G., Grosfils, E.B., Ayalew, D., Mohr, P., Zimbelman, J., and Ramsey, M., 2021, Magmatic rifting in the Main Ethiopian Rift began in thick continental lithosphere; the case of the Galema Range: Lithos, v. 406, p. 106494.

Class, C., Altherr, R., Volker, F., Eberz, G., and Mcculloch, M.T., 1994, Geochemistry of Pliocene to Quaternary alkali basalts from the Huri Hills, Northern Kenya: Chemical Geology, v. 113, p. 1–22.

Corti, G. et al., 2019, Aborted propagation of the Ethiopian rift caused by linkage with the Kenyan rift: Nature Communications, v. 10, p. 1309, doi:10.1038/s41467-019-09335-2.

Corti, G., 2009, Continental rift evolution: From rift initiation to incipient break-up in the Main Ethiopian Rift, East Africa: Earth-Science Reviews, v. 96, p. 1–53, doi:DOI 10.1016/j.earscirev.2009.06.005.

Corti, G., Bonini, M., Conticelli, S., Innocenti, F., Manetti, P., and Sokoutis, D., 2003, Analogue modelling of continental extension: a review focused on the relations between the patterns of deformation and the presence of magma: Earth-Science Reviews, v. 63, p. 169–247.

Davidson, A., 1983, The Omo River Project: Reconnaissance geology and geochemistry of parts of Illubabor, Kefa, Gemu Gofa, and Sidamo: Ethiopian Institute Geological Surveys Bulletin, v. 2, p. 1–89.

Davidson, A., and Rex, D.C., 1980, Age of Volcanism and Rifting in Southwestern Ethiopia: Nature, v. 283, p. 657–658.

Dunkelman, T.J., Karson, J.A., and Rosendahl, B.R., 1988, Structural style of the Turkana rift, Kenya: Geology, v. 16, p. 258–261.

Dunkelman, T.J., Rosendahl, B.R., and Karson, J.A., 1989, Structure and stratigraphy of the Turkana rift from seismic reflection data: Journal of African Earth Sciences (and the Middle East), v. 8, p. 489–510.

Dunkley, P.N., Smith, M., Allen, D.J., and Darling, W.G., 1993, The geothermal activity and geology of the northern sector of the Kenya Rift Valley:

Ebinger, C., 2005, Continental break-up: The East African perspective: Astronomy & Geophysics, v. 46, p. 16–21.

Ebinger, C.J., and Casey, M., 2001, Continental breakup in magmatic provinces: An Ethiopian example: Geology, v. 29, p. 527–530.

Ebinger, C.J., and Ibrahim, A., 1994, Multiple Episodes of Rifting in Central and East-Africa - a Reevaluation of Gravity-Data: Geologische Rundschau, v. 83, p. 689–702.

Ebinger, C.J., Keir, D., Bastow, I.D., Whaler, K., Hammond, J.O., Ayele, A., Miller, M.S., Tiberi, C., and Hautot, S., 2017, Crustal structure of active deformation zones in Africa: Implications for global crustal processes: Tectonics, v. 36, p. 3298–3332.

Ebinger, C.J., Yemane, T., Harding, D.J., Tesfaye, S., Kelley, S., and Rex, D.C., 2000, Rift deflection, migration, and propagation: Linkage of the Ethiopian and Eastern rifts, Africa: Geological Society of America Bulletin, v. 112, p. 163–176.

Ebinger, C.J., Yemane, T., WoldeGabriel, G., Aronson, J.L., and Walter, R.C., 1993, Late Eocene-Recent volcanism and faulting in the southern main Ethiopian Rift: Journal of the Geological Society of London, v. 150, p. 99–108.

Ernst, R.E., and Buchan, K.L., 2003, Recognizing mantle plumes in the geological record: Annual Review of Earth and Planetary Sciences, v. 31, p. 469–523.

Feibel, C.S., 2011, A geological history of the Turkana Basin: Evolutionary Anthropology: Issues, News, and Reviews, v. 20, p. 206–216.

Fitch, F.J., and Miller, J.A., 1976, Conventional potassium-argon and argon-40/argon-39 dating of volcanic rocks from East Rudolf: University of Chicago Press Chicago, p. 123–147.

Franceschini, Z., Cioni, R., Scaillet, S., Corti, G., Sani, F., Isola, I., Mazzarini, F., Duval, F., Erbello, A., and Muluneh, A., 2020, Recent volcano-tectonic activity of the Ririba rift and the evolution of rifting in South Ethiopia: Journal of Volcanology and Geothermal Research, v. 403, p. 106989.

Furman, T., Kaleta, K.M., Bryce, J.G., and Hanan, B.B., 2006, Tertiary mafic lavas of Turkana, Kenya: Constraints on East African plume structure and the occurrence of high-mu volcanism in Africa: Journal of Petrology, v. 47, p. 1221–1244.

Gathogo, P.N., Brown, F.H., and McDougall, I., 2008, Stratigraphy of the Koobi Fora Formation (Pliocene and Pleistocene) in the Loiyangalani region of northern Kenya: Journal of African Earth Sciences, v. 51, p. 277–297.

George, R.M., and Rogers, N.W., 2002, Plume dynamics beneath the African Plate inferred from the geochemistry of the Tertiary basalts of southern Ethiopia: Contributions to Mineralogy and Petrology, v. 144, p. 286–304.

George, R., Rogers, N., and Kelley, S., 1998, Earliest magmatism in Ethiopia: Evidence for two mantle plumes in one flood basalt province: Geology, v. 26, p. 923–926.

Gualda, G.A.R., Ghiorso, M.S., Lemons, R.V., and Carley, T.L., 2012, Rhyolite-MELTS: A modified calibration of MELTS optimized for silica-rich, fluid-bearing magmatic systems.: Journal of Petrology, p. doi:10.1093/petrology/egr080.

Guan, H., Geoffroy, L., and Xu, M., 2021, Magma-assisted fragmentation of Pangea: continental breakup initiation and propagation: Gondwana Research, v. 96, p. 56–75.

Guth, A.L., 2013, Spatial and Temporal Evolution of the Volcanics and Sediments of the Kenya Rift: Michigan Technological University.

Haileab, B., Brown, F.H., McDOUGALL, I., and Gathogo, P.N., 2004, Gombe Group basalts and initiation of Pliocene deposition in the Turkana depression, northern Kenya and southern Ethiopia: Geological Magazine, v. 141, p. 41–53.

Hayward, N.J., and Ebinger, C.J., 1996, Variations in the along-axis segmentation of the Afar Rift system: Tectonics, v. 15, p. 244–257.

Hendrie, D.B., Kusznir, N.J., Morley, C.K., and Ebinger, C.J., 1994, Cenozoic extension in Northern Kenya - A quantitative model of rift basin development in the Turkana region: Tectonophysics, v. 236, p. 409–438.

Humphreys, M.C.S., Edmonds, M., Plail, M., Barclay, J., Parkes, D., and Christopher, T., 2013, A new method to quantify the real supply of mafic components to a hybrid andesite: Contributions to Mineralogy and Petrology, v. 165, p. 191–215.

JICA, 2012, Geological Map of Konso - Yabelo Area: Japan International Copperation Agency (JICA) The Study on Groundwater Resources Assessment in the Rift Valley Lakes Basin.

Karson, J.A., and Curtis, P.C., 1989, Tectonic and magmatic processes in the Eastern Branch of the East African Rift and implications for magmatically active continental rifts: Journal of African Earth Sciences (and the Middle East), v. 8, p. 431–453, doi:http://dx.doi.org/10.1016/S0899-5362(89)80037-5.

Katz, R.F., Spiegelman, M., and Langmuir, C.H., 2003, A new parameterization of hydrous mantle melting: Geochemistry, Geophysics, Geosystems, v. 4.

Keir, D., Bastow, I.D., Pagli, C., and Chambers, E.L., 2013, The development of extension and magmatism in the Red Sea rift of Afar: Tectonophysics, v. 607, p. 98–114, doi:http://dx.doi.org/10.1016/j.tecto.2012.10.015.

Key, R.M., Rop, B.P., and Rundle, C.C., 1987, The development of the late Cenozoic alkali basaltic Marsabit Shield-Volcano, Northern Kenya: Journal of African Earth Sciences, v. 6, p. 475–491.

Key, R.M., and Watkins, R.T., 1988, Geology of the Sabarei area: Republic of Kenya Ministry of Environment and Natural Resources, Mines and Geological Department Report, v. 111.

Kimura, J.-I., and Kawabata, H., 2014, Trace element mass balance in hydrous adiabatic mantle melting: The Hydrous Adiabatic Mantle Melting Simulator version 1 (HAMMS1): Geochemistry, Geophysics, Geosystems, v. 15, p. 2467–2493.

Kitagawa, H., Kobayashi, K., Makishima, A., and Nakamura, E., 2008, Multiple pulses of the mantle plume: evidence from Tertiary Icelandic lavas: Journal of Petrology, v. 49, p. 1365–1396.

Knappe, E., Bendick, R., Ebinger, C., Birhanu, Y., Lewi, E., Floyd, M., King, R., Kianji, G., Mariita, N., and Temtime, T., 2020, Accommodation of East African Rifting across the Turkana Depression: Journal of Geophysical Research: Solid Earth, v. 125, p. e2019JB018469.

Kounoudis, R., Bastow, I.D., Ebinger, C.J., Darbyshire, F., Ogden, C.S., Musila, M., Ugo, F., Ayele, A., Sullivan, G., and Bendick, R., 2023, The development of rifting and magmatism in the multiply rifted Turkana Depression, East Africa: Evidence from surface-wave analysis of crustal and uppermost mantle structure: Earth and Planetary Science Letters, v. 621, p. 118386.

Kounoudis, R., Bastow, I.D., Ebinger, C.J., Ogden, C.S., Ayele, A., Bendick, R., Mariita, N., Kianji, G., Wigham, G., and Musila, M., 2021, Body-Wave Tomographic Imaging of the Turkana Depression: Implications for Rift Development and Plume-Lithosphere Interactions: Geochemistry, Geophysics, Geosystems, v. 22, p. e2021GC009782.

Krans, S.R., Rooney, T.O., Kappelman, J., Yirgu, G., and Ayalew, D., 2018, From initiation to termination: a petrostratigraphic tour of the Ethiopian Low-Ti Flood Basalt Province: Contributions to Mineralogy and Petrology, v. 173, p. 37, doi:10.1007/s00410-018-1460-7.

Lahitte, P., Gillot, P.-Y., Kidane, T., Courtillot, V., and Bekele, A., 2003, New age constraints on the timing of volcanism in central Afar, in the presence of propagating rifts: Journal of Geophysical Research: Solid Earth, v. 108, p. 2123, doi:10.1029/2001jb001689.

Lee, C.-T.A., Luffi, P., Plank, T., Dalton, H., and Leeman, W.P., 2009, Constraints on the depths and temperatures of basaltic magma generation on Earth and other terrestrial planets using new thermobarometers for mafic magmas: Earth and Planetary Science Letters, v. 279, p. 20–33.

Macgregor, D., 2015, History of the development of the East African Rift System: A series of interpreted maps through time: Journal of African Earth Sciences, v. 101, p. 232–252.

Mazzarini, F., Corti, G., Manetti, P., and Innocenti, F., 2004, Strain rate and bimodal volcanism in the continental rift: Debre Zeyt volcanic field, northern MER, Ethiopia: Journal of African Earth Sciences, v. 39, p. 415–420, doi:DOI 10.1016/j.jafrearsci.2004.07.025.

McDougall, I.A.N., and Brown, F.H., 2008, Geochronology of the pre-KBS tuff sequence, Omo Group, Turkana Basin: Journal of the Geological Society, v. 165, p. 549–562.

McDougall, I., and Brown, F.H., 2009, Timing of volcanism and evolution of the northern Kenya Rift: Geological Magazine, v. 146, p. 34–47.

McDougall, I., and Feibel, C.S., 1999, Numerical age control for the Miocene-Pliocene succession at Lothagam, a hominoid-bearing sequence in the northern Kenya Rift: Journal of the Geological Society, v. 156, p. 731–745, doi:10.1144/gsjgs.156.4.0731.

McDougall, I., and Watkins, R.T., 2006, Geochronology of the Nabwal Hills: a record of earliest magmatism in the northern Kenyan Rift Valley: Geological Magazine, v. 143, p. 25–39.

McDougall, I., and Watkins, R.T., 1988, Potassium–argon ages of volcanic rocks from northeast of Lake Turkana, northern Kenya: Geological Magazine, v. 125, p. 15–23.

McKenzie, D., and Bickle, M.J., 1988, The volume and composition of melt generated by extension of the lithosphere: Journal of Petrology, v. 29, p. 625–679.

Mechie, J., Keller, G.R., Prodehl, C., Khan, M.A., and Gaciri, S.J., 1997, A model for the structure, composition and evolution of the Kenya rift: Tectonophysics, v. 278, p. 95–119.

Mohr, P., 1983, Ethiopian flood basalt province: Nature, v. 303, p. 577–584.

Morley, C.K., 2020, Early syn-rift igneous dike patterns, northern Kenya Rift (Turkana, Kenya): Implications for local and regional stresses, tectonics, and magma-structure interactions: Geosphere, v. 16, p. 890–918.

Morley, C.K., 1994, Interaction of deep and shallow processes in the evolution of the Kenya rift: Tectonophysics, v. 236, p. 81–91.

Morley, C.K., 2010, Stress re-orientation along zones of weak fabrics in rifts: An explanation for pure extension in 'oblique'rift segments? Earth and Planetary Science Letters, v. 297, p. 667–673.

Morley, C.K., Bosworth, W., Day, R.A., Lauck, R., Bosher, R., Stone, D.M., Wigger, S.T., Wescott, W.A., Haun, D., and Bassett, N., 1999a, AAPG Studies in Geology# 44, Chapter 4: Geology and Geophysics of the Anza Graben:

Morley, C.K., Karanja, F.M., Wescott, W.A., Stone, D.M., Harper, R.M., Wigger, S.T., and Day, R.A., 1999b, Chapter 2: Geology and Geophysics of the Western Turkana Basins, Kenya, *in* Geoscience of Rift Systems—Evolution of East African. C.K. Morely (ed), AAPG, AAPG Studies in Geology, v. 44, p. 19–54.

Morley, C.K., Ngenoh, D.K., and Ego, J.K., 1999c, Chapter 1: Introduction to the East African Rift System, *in* Geoscience of Rift Systems—Evolution of East Africa, C.K. Morely (ed), AAPG, AAPG Studies in Geology, v. 44, p. 1–18.

Morley, C.K., Wescott, W.A., Stone, D.M., Harper, R.M., Wigger, S.T., and Karanja, F.M., 1992, Tectonic evolution of the Northern Kenyan rift: Journal of the Geological Society, v. 149, p. 333–348.

Muirhead, J.D., Scholz, C.A., and O. Rooney, T., 2022, Transition to magma-driven rifting in the South Turkana Basin, Kenya: Part 1: Journal of the Geological Society, v. 179, p. jgs2021-159.

Musila, M., Ebinger, C.J., Bastow, I.D., Sullivan, G., Oliva, S.J., Knappe, E., Perry, M., Kounoudis, R., Ogden, C.S., and Bendick, R., 2023, Active Deformation Constraints on the Nubia-Somalia Plate Boundary Through Heterogenous Lithosphere of the Turkana Depression: Geochemistry, Geophysics, Geosystems, v. 24, p. e2023GC010982.

Ochieng, J.O., Wilkinson, A.F., Kenya. Ministry of Environment, and Natural Resources, 1988, Geology of the Loiyangalani Area: Degree: Ministry of Environment and Natural Resources.

Ogden, C.S., Bastow, I.D., Ebinger, C., Ayele, A., Kounoudis, R., Musila, M., Bendick, R., Mariita, N., Kianji, G., and Rooney, T.O., 2023, The development of multiple phases of superposed rifting in the Turkana Depression, East Africa: Evidence from receiver functions: Earth and Planetary Science Letters, v. 609, p. 118088.

Opdyke, N.D., Kent, D.V., Huang, K., Foster, D.A., and Patel, J.P., 2010, Equatorial paleomagnetic time-averaged field results from 0–5 Ma lavas from Kenya and the latitudinal variation of angular dispersion: Geochemistry, Geophysics, Geosystems, v. 11.

Pedersen, T., and van der Beek, P., 1994, Extension and magmatism in the Oslo Rift, southeast Norway: no sign of a mantle plume: Earth and Planetary Science Letters, v. 123, p. 317–329.

Pedersen, T., and Ro, H.E., 1992, Finite duration extension and decompression melting: Earth and planetary science letters, v. 113, p. 15–22.

Pik, R., Deniel, C., Coulon, C., Yirgu, G., and Marty, B., 1999, Isotopic and trace element signatures of Ethiopian flood basalts; evidence for plume-lithosphere interactions: Geochimica Et Cosmochimica Acta, v. 63, p. 2263–2279.

Pilet, S., Baker, M.B., and Stolper, E.M., 2008, Metasomatized Lithosphere and the Origin of Alkaline Lavas: Science, v. 320, p. 916–919, doi:10.1126/science.1156563.

Prodehl, C., Ritter, J.R.R., Mechie, J., Keller, G.R., Khan, M.A., Jacob, B., Fuchs, K., Nyambok, I.O., Obel, J.D., and Riaroh, D., 1997, The KRISP 94 lithospheric investigation of southern Kenya—the experiments and their main results: Tectonophysics, v. 278, p. 121–147.

Purcell, P.G., 2018, Re-imagining and re-imaging the development of the East African Rift: Petroleum Geoscience, v. 24, p. 21–40.

Reeves, C.V., Karanja, F.M., and MacLeod, I.N., 1987, Geophysical evidence for a failed Jurassic rift and triple junction in Kenya: Earth and Planetary Science Letters, v. 81, p. 299–311.

Rooney, T.O., 2020a, The Cenozoic magmatism of East Africa: Part II–Rifting of the mobile belt: Lithos, v. 360, p. 105291, doi:10.1016/j.lithos.2019.105291.

Rooney, T.O., 2020b, The Cenozoic magmatism of East Africa: part V–magma sources and processes in the East African Rift: Lithos, v. 360, p. 105296, doi:doi: 10.1016/j.lithos.2019.105296.

Rooney, T.O., 2017, The Cenozoic magmatism of East-Africa: Part I—flood basalts and pulsed magmatism: Lithos, v. 286, p. 264–301.

Rooney, T.O., Bastow, I.D., Keir, D., Mazzarini, F., Movsesian, E., Grosfils, E.B., Zimbelman, J.R., Ramsey, M.S., Ayalew, D., and Yirgu, G., 2014, The protracted development of focused magmatic intrusion during continental rifting: Tectonics, v. 33, p. 875–897, doi:DOI: 10.1002/2013TC003514.

Rooney, T.O., Brown, E.L., Bastow, I.D., Arrowsmith, J.R., and Campisano, C.J., 2023, Magmatism during the continent–ocean transition: Earth and Planetary Science Letters, v. 614, p. 118189.

Rooney, T.O., Hanan, B.B., Graham, D.W., Furman, T., Blichert-Toft, J., and Schilling, J.-G., 2012a, Upper Mantle Pollution during Afar Plume–Continental Rift Interaction: Journal of Petrology, v. 53, p. 365–389, doi:10.1093/petrology/egr065.

Rooney, T.O., Hart, W.K., Hall, C.M., Ayalew, D., Ghiorso, M.S., Hidalgo, P., and Yirgu, G., 2012b, Peralkaline magma evolution and the tephra record in the Ethiopian Rift: Contributions to Mineralogy and Petrology, v. 164, p. 407–426.

Rooney, T.O., Herzberg, C., and Bastow, I.D., 2012c, Elevated mantle temperature beneath East Africa: Geology, v. 40, p. 27–30, doi:10.1130/g32382.1.

Rooney, T.O., Wallace, P.J., Muirhead, J.D., Chiasera, B., Steiner, R.A., Girard, G., and Karson, J.A., 2022, Transition to magma-driven rifting in the South Turkana Basin, Kenya: Part 2: Journal of the Geological Society, v. 179, p. jgs2021-160.

Schneider, C.A., Rasband, W.S., and Eliceiri, K.W., 2012, NIH Image to ImageJ: 25 years of image analysis: Nature methods, v. 9, p. 671–675.

Schofield, N., Newton, R., Thackrey, S., Watson, D., Jolley, D., and Morley, C., 2021, Linking surface and subsurface volcanic stratigraphy in the Turkana Depression of the East African Rift system: Journal of the Geological Society, v. 178, p. jgs2020-110.

Shinjo, R., Chekol, T., Meshesha, D., Itaya, T., and Tatsumi, Y., 2011, Geochemistry and geochronology of the mafic lavas from the southeastern Ethiopian rift (the East African Rift System): assessment of models on magma sources, plume–lithosphere interaction and plume evolution: Contributions to Mineralogy and Petrology, v. 162, p. 209–230.

Simiyu, S.M., and Keller, G.R., 1997, An integrated analysis of lithospheric structure across the East African plateau based on gravity anomalies and recent seismic studies: Tectonophysics, v. 278, p. 291–313.

Stab, M., Bellahsen, N., Pik, R., Quidelleur, X., Ayalew, D., and Leroy, S., 2016, Modes of rifting in magma-rich settings: Tectono-magmatic evolution of Central Afar: Tectonics, v. 35, p. 2–38, doi:10.1002/2015tc003893.

Steiner, R.A., and Rooney, T.O., 2021, PiAutoStage: An Open-Source 3D Printed Tool for the Automatic Collection of High-Resolution Microscope Imagery: Geochemistry, Geophysics, Geosystems, v. 22, p. e2021GC009693.

Steiner, R.A., Rooney, T.O., Girard, G., Rogers, N.W., Ebinger, C., Peterson, L., and Phillips, R., 2021, Cenozoic Magmatic Activity in East Africa: New Geochemical Constraints on Magma Distribution within the Eocene Continental Flood Basalt Province, *in* Large Igneous Provinces and their Plumbing Systems, Journal of the Geological Society Special Publications 518, 518.

Steiner, R.A., Rooney, T.O., Kappelman, J., Lydic, T., Girard, G., Mariita, N., and Phillips, R., 2024, Messengers from the Magma Chambers: Petro-Stratigraphic Analysis of Plagioclase-Rich Flood Basalt Lavas in Turkana, Kenya: Journal of Petrology, p. egae044.

Stewart, K., and Rogers, N., 1996, Mantle plume and lithosphere contributions to basalts from southern Ethiopia: Earth and Planetary Science Letters, v. 139, p. 195–211.

Thy, P., 1983, Phase relations in transitional and alkali basaltic glasses from Iceland: Contributions to Mineralogy and Petrology, v. 82, p. 232–251.

Vetel, W., and Le Gall, B., 2006, Dynamics of prolonged continental extension in magmatic rifts: the Turkana Rift case study (North Kenya): Geological Society, London, Special Publications, v. 259, p. 209–233.

Watkins, R.T., 1986, Volcano-tectonic control on sedimentation in the Koobi Fora sedimentary basin, Lake Turkana: Geological Society, London, Special Publications, v. 25, p. 85–95.

Wescott, W.A., Wigger, S.T., Stone, D.M., and Morley, C.K., 1999, Geology and geophysics of the Lotikipi Plain: Geoscience of Rift Systems-Evolution of East Africa, American Association of Petroleum Geologists Studies in Geology, v. 44, p. 55–65.

Wilson, M., Neumann, E.-R., Davies, G.R., Timmerman, M.J., Heeremans, M., and Larsen, B.T., 2004, Permo-Carboniferous magmatism and rifting in Europe: introduction: Geological Society, London, Special Publications, v. 223, p. 1–10.

Wolfenden, E., Ebinger, C., Yirgu, G., Renne, P.R., and Kelley, S.P., 2005, Evolution of a volcanic rifted margin: Southern Red Sea, Ethiopia: Geological Society of America Bulletin, v. 117, p. 846–864.

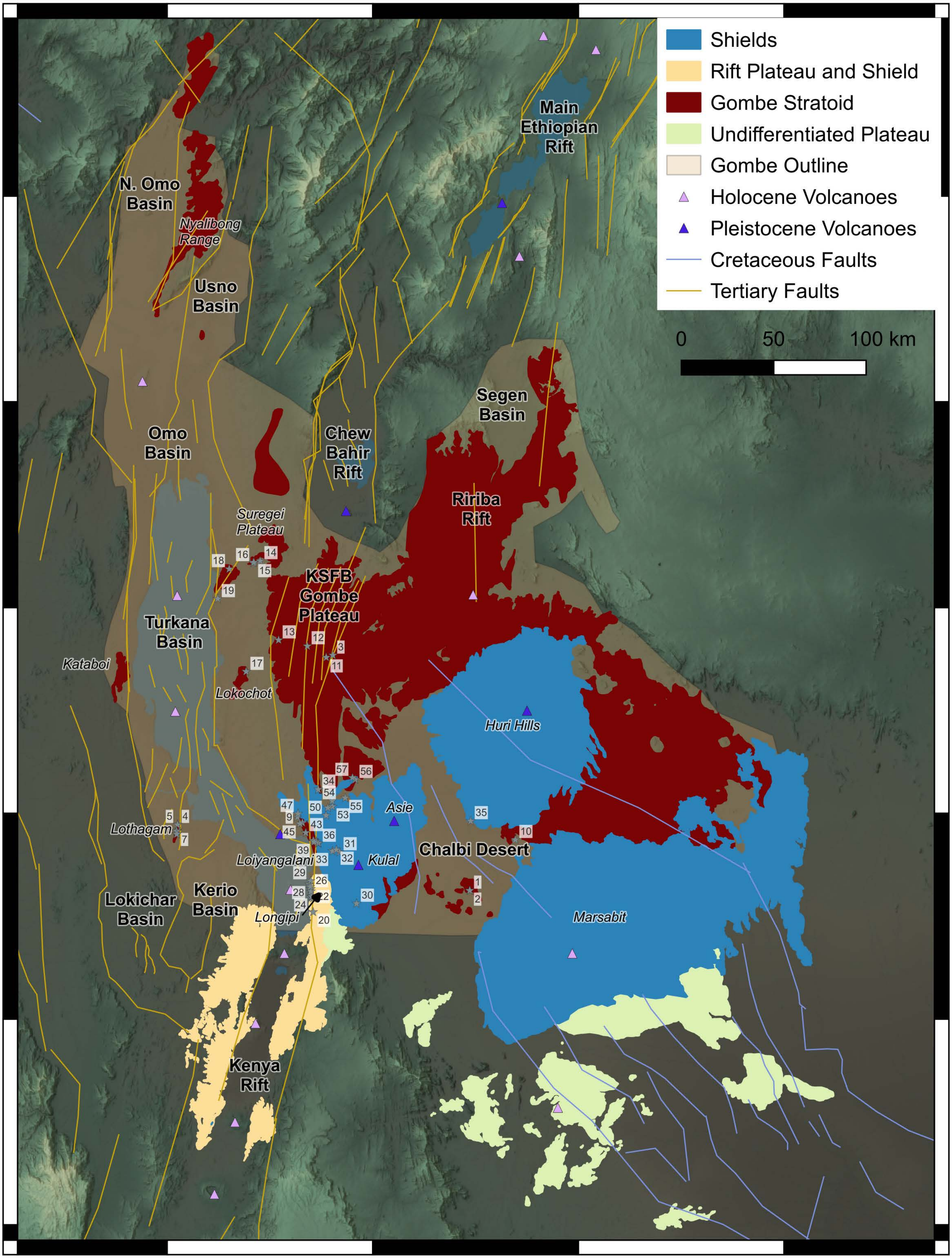

Shields
Rift Plateau and Shield
Gombe Stratoid
Undifferentiated Plateau
Gombe Outline
Holocene Volcanoes
Pleistocene Volcanoes
Cretaceous Faults
Tertiary Faults
0
50
100 km
Main Ethiopian Rift
N. Omo Basin
Nyalibong Range
Usno Basin
Omo Basin
Chew Bahir Rift
Segen Basin
Ririba Rift
Suregei Plateau
KSFB Gombe Plateau
Turkana Basin
Kataboi
Lokochot
Huri Hills
Asie
Lothagam
Loiyangalani
Kulal
Chalbi Desert
Lokichar Basin
Kerio Basin
Longipi
Marsabit
Kenya Rift
6°N
5°N
4°N
3°N
2°N
1°N
36°E
37°E
38°E
39°E

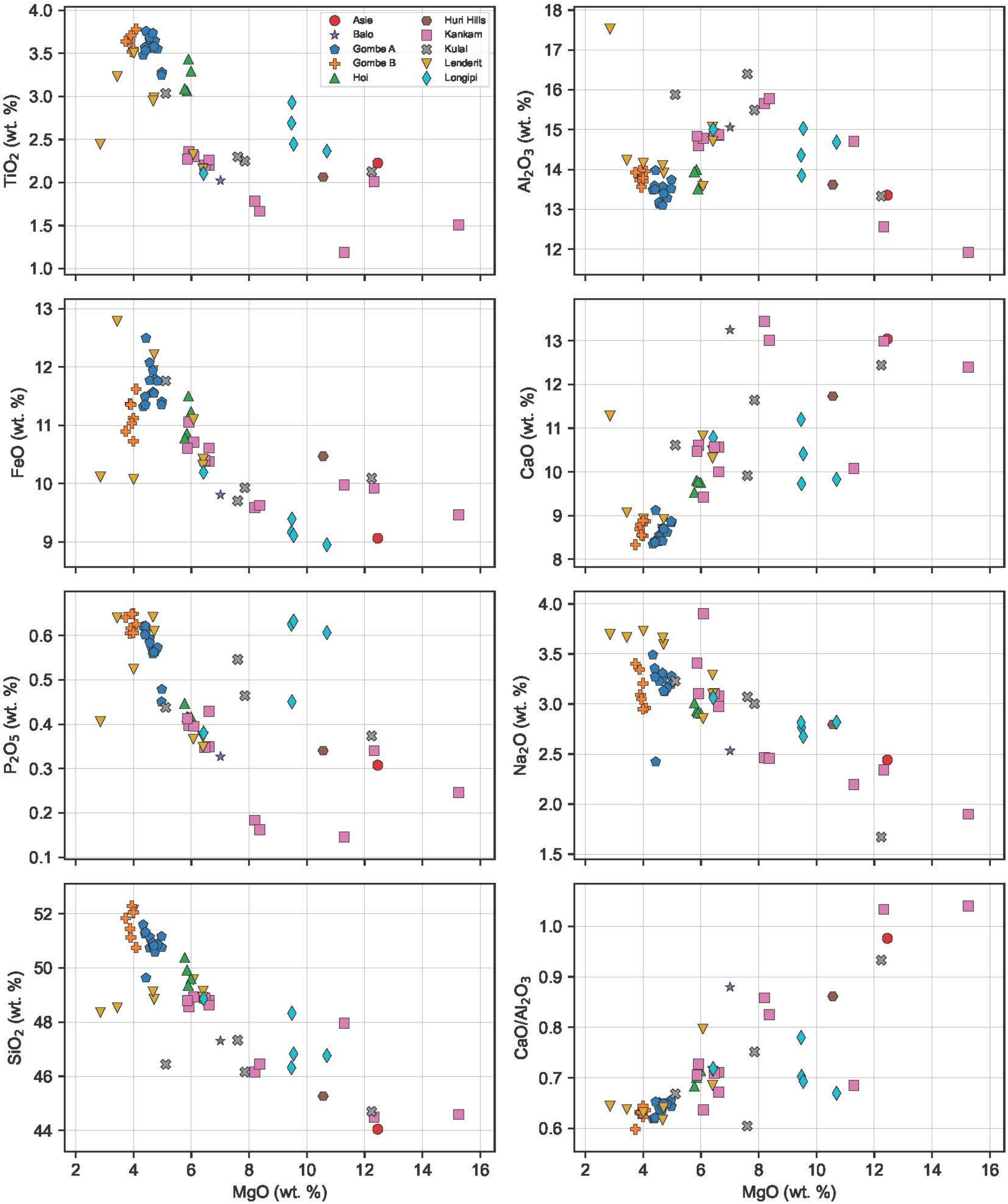

Asie
Balo
Gombe A
Gombe B
Hoi
Huri Hills
Kankam
Kulal
Lenderit
Longipi
TiO2 (wt. %)
Al2O3 (wt. %)
FeO (wt. %)
CaO (wt. %)
P2O5 (wt. %)
Na2O (wt. %)
SiO2 (wt. %)
CaO/Al2O3
MgO (wt. %)
MgO (wt. %)

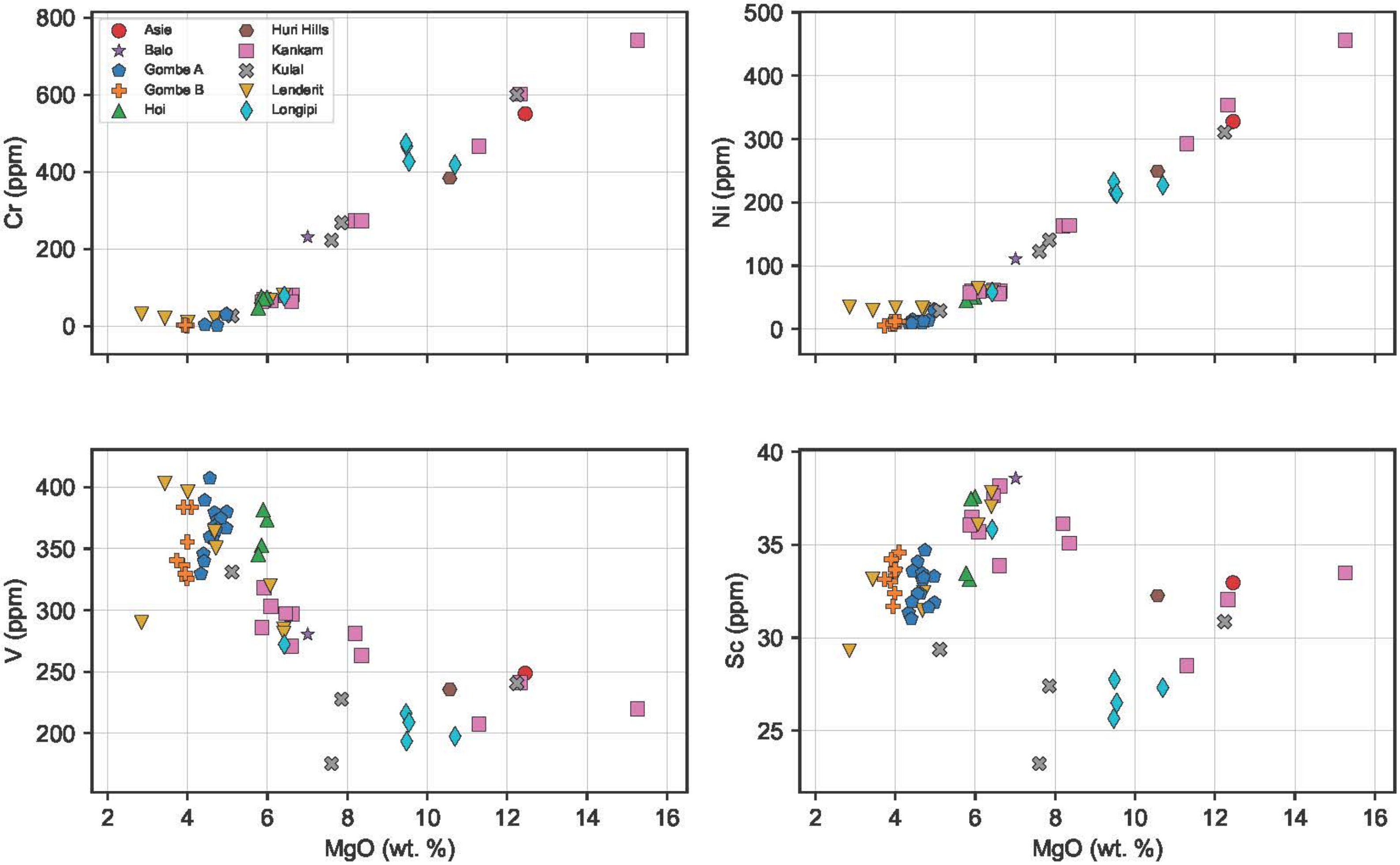
Asie
Balo
Gombe A
Gombe B
Hoi
Huri Hills
Kankam
Kulal
Lenderit
Longipi
Cr (ppm)
Ni (ppm)
V (ppm)
Sc (ppm)
MgO (wt. %)
MgO (wt. %)

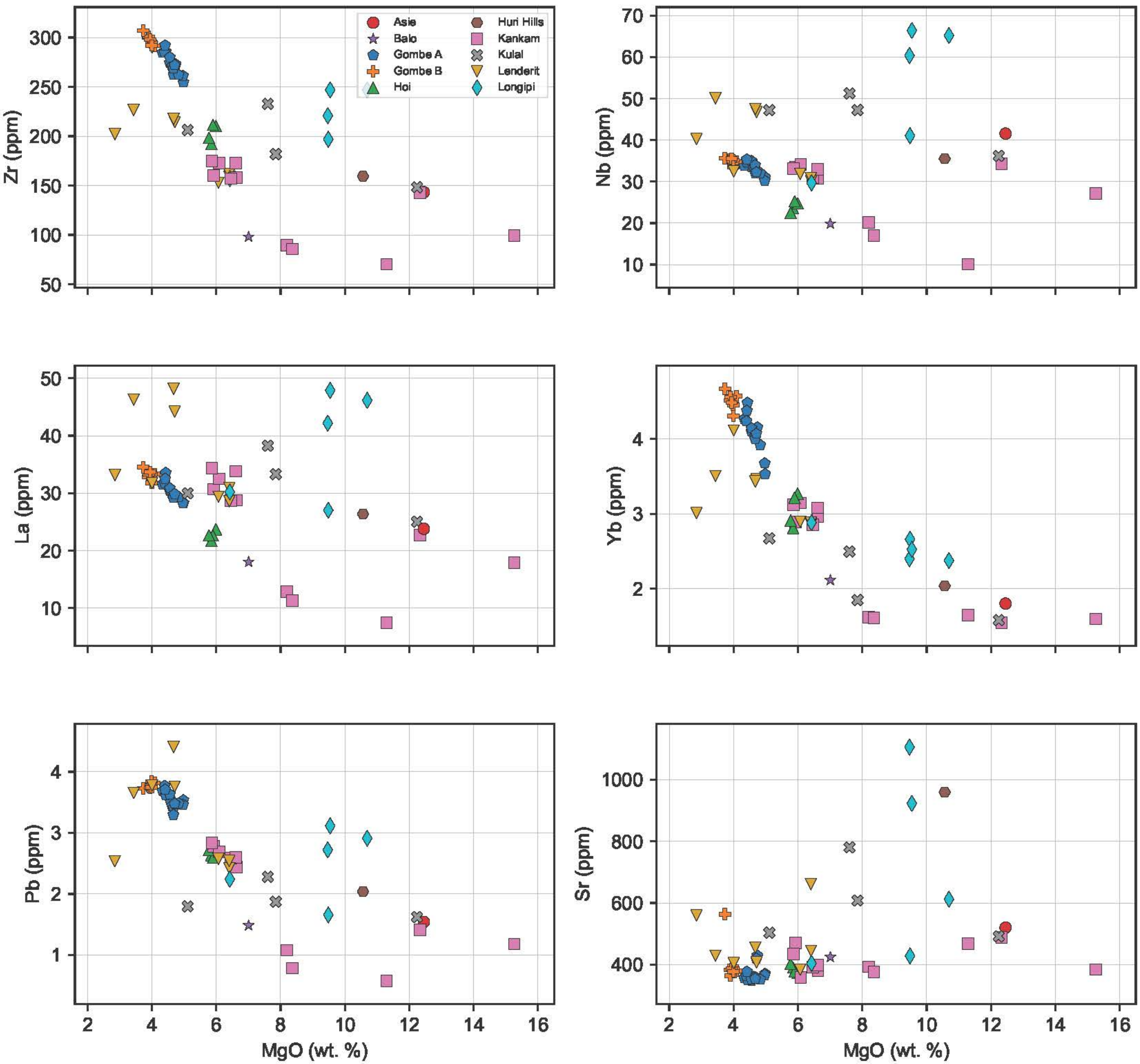
Asie
Balo
Gombe A
Gombe B
Hoi
Huri Hills
Kankam
Kulal
Lenderit
Longipi
Zr (ppm)
Nb (ppm)
La (ppm)
Yb (ppm)
Pb (ppm)
Sr (ppm)
MgO (wt. %)
MgO (wt. %)

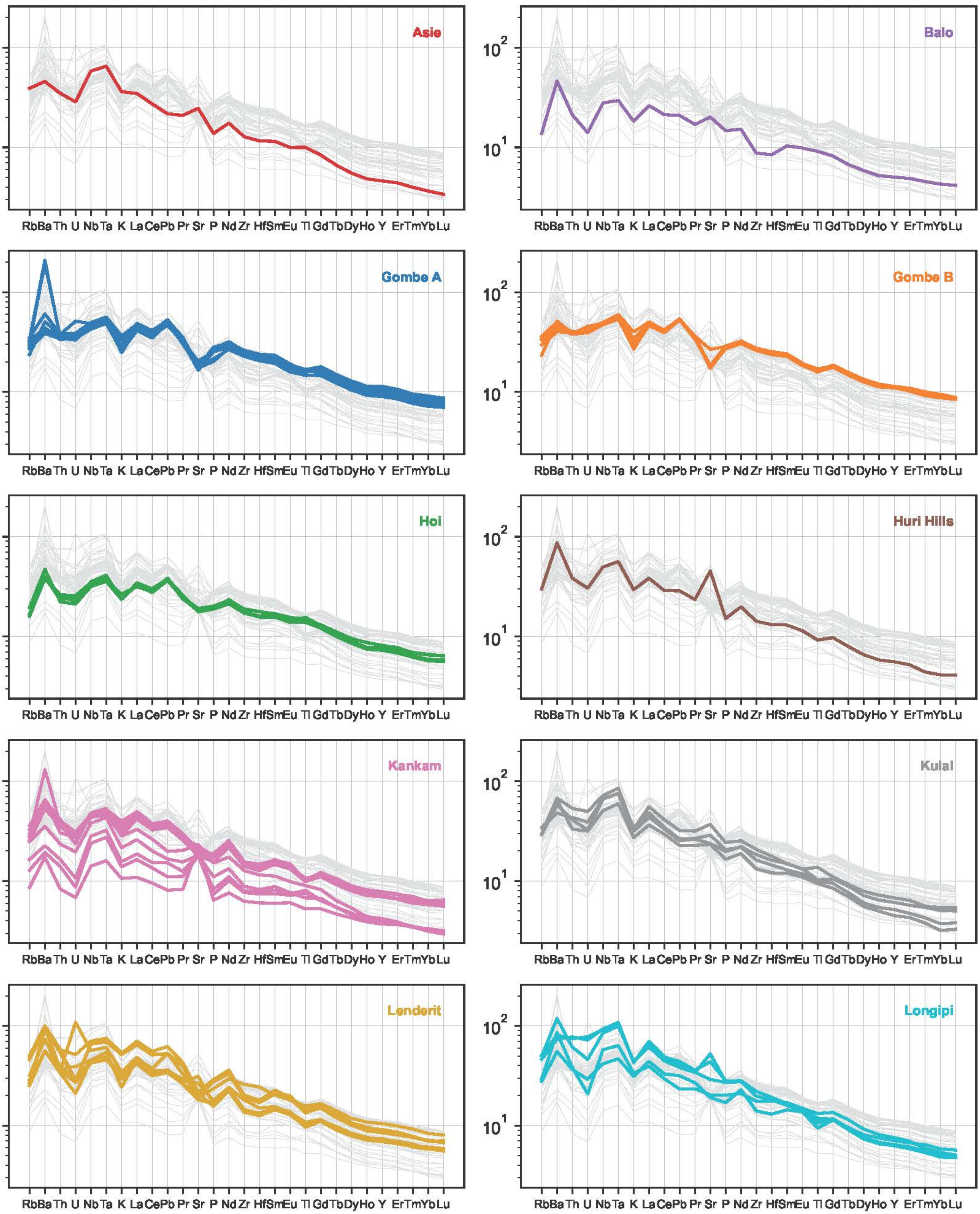
Asie
Balo
Gombe A
Gombe B
Hoi
Huri Hills
Kankam
Kulal
Lenderit
Longipi
10^2
10^1
Rb Ba Th U Nb Ta K La Ce Pb Pr Sr P Nd Zr Hf Sm Eu Ti Gd Tb Dy Ho Y Er Tm Yb Lu

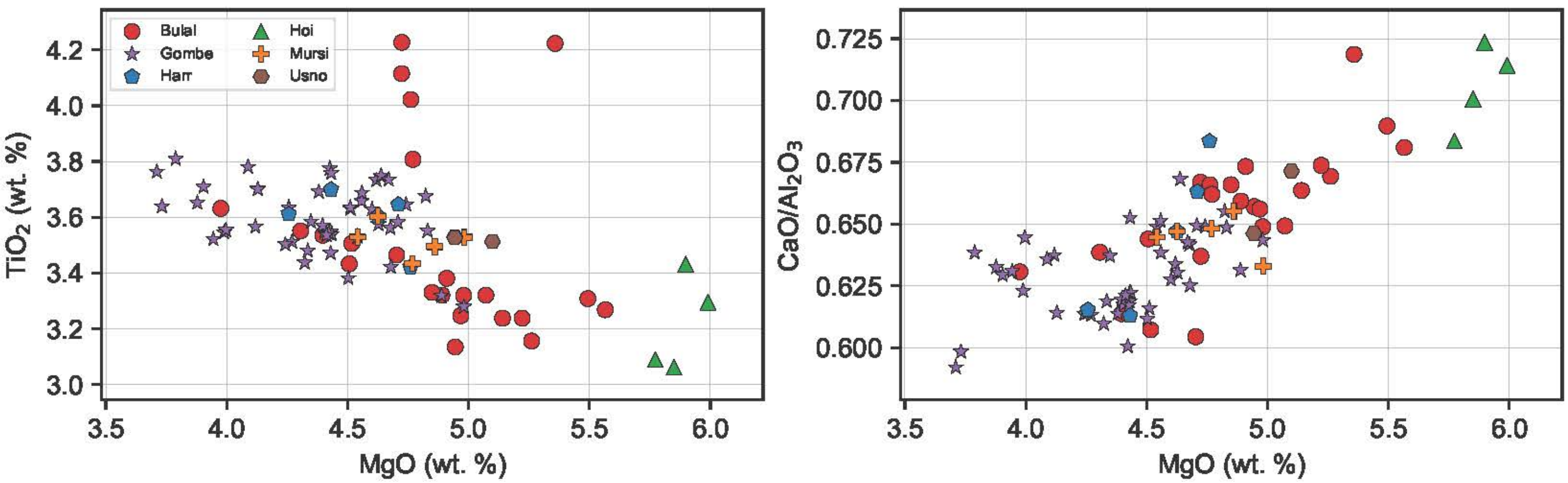
Bulal
Gombe
Harr
Hoi
Mursi
Usno
4.2
4.0
3.8
3.6
3.4
3.2
3.0
TiO2 (wt. %)
3.5
4.0
4.5
5.0
5.5
6.0
MgO (wt. %)
0.725
0.700
0.675
0.650
0.625
0.600
CaO/Al2O3
MgO (wt. %)

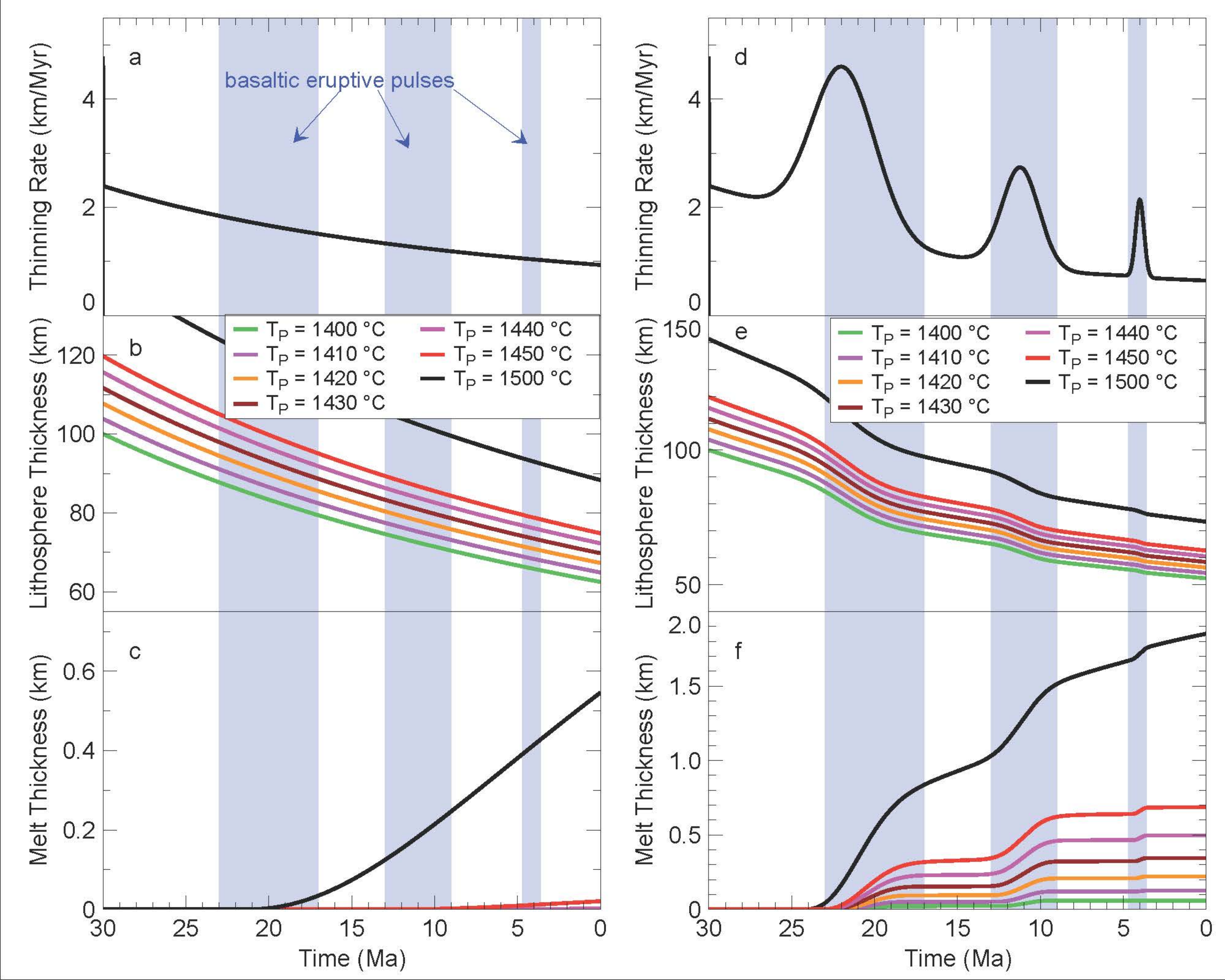

a
basaltic eruptive pulses
Thinning Rate (km/Myr)
b
Lithosphere Thickness (km)
T_P = 1400 °C
T_P = 1410 °C
T_P = 1420 °C
T_P = 1430 °C
T_P = 1440 °C
T_P = 1450 °C
T_P = 1500 °C
c
Melt Thickness (km)
Time (Ma)
d
Thinning Rate (km/Myr)
e
Lithosphere Thickness (km)
f
Melt Thickness (km)
Time (Ma)

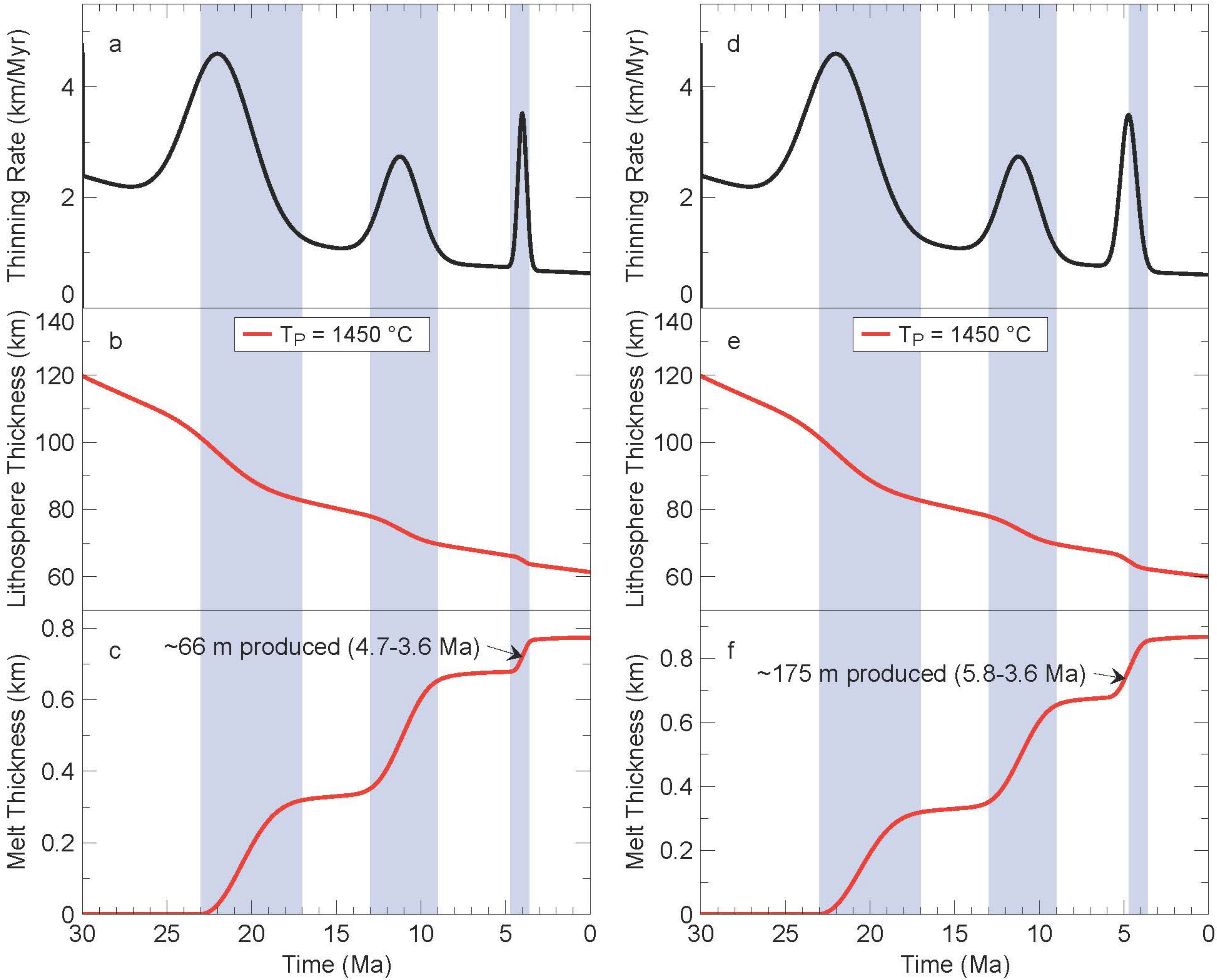

a
b
c
d
e
f
Thinning Rate (km/Myr)
Lithosphere Thickness (km)
Melt Thickness (km)
Time (Ma)
T_P = 1450 °C
~66 m produced (4.7-3.6 Ma)
~175 m produced (5.8-3.6 Ma)

Sample (IGSN)	TOR0000O1	TOR0001D8	TOR0001D9	TOR0001DK	TOR0001DL
T (°C) major elements (Lee et al. 2009) (Fe^{3+}/Fe_{total} = 0.15)	1432	1512	1453	1441	1480
T (°C) major elements (Lee et al. 2009) (Fe^{3+}/Fe_{total} = 0.05)	1490	1573	1510	1496	1537
P (GPa) major elements (Lee et al. 2009) (Fe^{3+}/Fe_{total} = 0.15)	2.10	3.12	2.47	2.51	2.87
P (GPa) major elements (Lee et al. 2009) (Fe^{3+}/Fe_{total} = 0.05)	2.6	3.8	3.0	3.0	3.5
Calculated depth of melt equilibration (km) (Fe^{3+}/Fe_{total} = 0.15)	74	109	86.9	88.4	101.2
Calculated depth of melt equilibration (km) (Fe^{3+}/Fe_{total} = 0.05)	91.4	133.6	105.5	105.5	123
Calculated T_P (°C) (Fe^{3+}/Fe_{total} = 0.15)	1405	1471	1421	1408	1442
Calculated T_P (°C) (Fe^{3+}/Fe_{total} = 0.05)	1455	1522	1470	1455	1490
T_P (°C) trace elements (HAMMS)	1430	1450	1390	1430	1400
Pressure (GPa) trace elements	2.9	3.5	2.9	3.2	3.1
H_2O content (wt. %)	0	0	0.01	0	0.01
CsDep	0.8	0.1	0.2	0.5	0.2
Fcont	4	1	3	4	2
Calculated depth of melting (km)	102	123	102	112.5	109

Table 1.